Title

- **Long title**: Proteins Derived From MRL/MpJ Tendon Provisional Extracellular Matrix and Secretome Promote Pro-Regenerative Tenocyte Behavior
- **Short title**: MRL Proteins Promote a Pro-Regenerative Phenotype

Authors

Jason C. Marvin,[1] Ethan J. Liu,[2] Hsin Huei Chen,[2] David A. Shiovitz[3], Nelly Andarawis-Puri[2,4]*

Affiliations

[1]Nancy E. and Peter C. Meinig School of Biomedical Engineering, Cornell University, Ithaca, NY 14853, USA

[2]Sibley School of Mechanical and Aerospace Engineering, Cornell University, Cornell University, Ithaca, NY 14853, USA

[3]Phelps Hospital, Tarrytown, NY 10591, USA

[4]Hospital for Special Surgery, New York, NY, USA

*Corresponding author: na424@cornell.edu

Abstract

Tendinopathies are prevalent musculoskeletal conditions that have no effective therapies to attenuate scar formation. In contrast to other adult mammals, the tendons of Murphy Roths Large (MRL/MpJ) mice possess a superior healing capacity following acute and overuse injuries. Here, we hypothesized that the application of biological cues derived from the local MRL/MpJ tendon environment would direct otherwise scar-mediated tenocytes towards a pro-regenerative MRL/MpJ-like phenotype. We identified soluble factors enriched in the secretome of MRL/MpJ tenocytes using bioreactor systems and quantitative proteomics. We then demonstrated that the combined administration of structural and soluble constituents isolated from decellularized MRL/MpJ tendon provisional ECM (dPECM) and the secretome stimulate scar-mediated rodent tenocytes towards enhanced mechanosensitivity, proliferation, intercellular communication, and ECM deposition associated with MRL/MpJ cell behavior. Our findings highlight key biological mechanisms that drive MRL/MpJ tenocyte activity and their interspecies utility to be harnessed for therapeutic strategies that promote pro-regenerative healing outcomes.

Teaser

Proteins enriched in a super-healer mouse strain elicit interspecies utility in promoting pro-regenerative tenocyte behavior.

MAIN TEXT

Introduction

Tendinopathies are debilitating disorders that account for over a third of all musculoskeletal consultations (1). In adult mammals, tendon ruptures heal poorly by forming fibrovascular and mechanically inferior scar tissue ('scar-mediated healing') that

is later remodeled ineffectively by resident tendon cells, or tenocytes. This scar-mediated healing can result in long-term pain, disability, and functional deficits that contribute to a reduced quality of life. Surgical repair remains the gold standard for the clinical treatment of tendon ruptures wherein the torn ends are reattached to restore load transmission and the original tissue functionality. However, these procedures do not address the underlying pathology and suffer from post-operative re-tear rates as high as 94% (2–4). The use of biologic therapies, such as autologous platelet-rich plasma (PRP) injections, to promote tendon healing remains contentious given variable reports of their clinical efficacy in attenuating scar-mediated healing (5,6), which is attributed to a lack of standardization in their manufacturing, quality control, and administration. Clearly, a better understanding the biological mechanisms underpinning tendon regeneration is critical to development of more effective therapeutics.

The Murphy Roths Large (MRL/MpJ) mouse strain harbors a natural regenerative capacity in several tissues and organs (7,8), including tendon (9–15). We have previously shown that MRL/MpJ tendons exhibit vastly improved structural and mechanical recovery as compared to canonical healing C57BL/6 (B6) tendons following acute laceration/full-thickness hole punch or overuse injuries (9,12,13), thereby establishing the promise of the MRL/MpJ mouse strain for expanding our mechanistic understanding of scarless tendon healing. Using *ex vivo* organ culture to eliminate any systemic contributions to healing, we previously found that hole-punched MRL/MpJ tendons showed significantly increased bulk mechanical properties compared to those of B6 tendons at 4 weeks post-injury (wpi). These findings suggest that the local tendon environment consisting of resident tenocytes and the extracellular matrix (ECM) primarily drive MRL/MpJ scarless tendon healing (11,12), which raised the question of whether the MRL/MpJ tendon ECM can ameliorate otherwise scar-mediated healing outcomes. Subsequent *in vivo* assessment of the therapeutic utility of a PEG-4MAL hydrogel incorporated with decellularized MRL/MpJ tendon provisional ECM (dPECM), a temporary bioactive ECM produced during the proliferative phase of healing, improved B6 tendon alignment, cell elongation, and stiffness compared to untreated tendons by 6 weeks post-implantation (16). Moreover, in that study, we identified a subset of proteins that are uniquely enriched in the MRL/MpJ tendon dPECM that may contribute to these improved healing outcomes. However, native tissue mechanical properties were not fully recovered despite the enhanced structure achieved using these dPECM constructs. While decellularization of tissue samples for dPECM collection is necessary to prevent immunogenicity, this technique removes resident tenocytes and most of their direct contributions within the tendon. These findings suggest that supplementation of tenocyte-secreted soluble factors, otherwise known as the secretome, may augment the therapeutic potency of the MRL/MpJ tendon dPECM.

This study aims to (*i*) comparatively characterize B6 and MRL/MpJ tenocyte behavior to establish robust cellular metrics that delineate scar-mediated and scarless tendon healing, (*ii*) identify soluble factors enriched in the MRL/MpJ tenocyte secretome, and (*iii*) determine whether the administration of MRL/MpJ-enriched soluble and ECM proteins together is functionally advantageous in stimulating pro-regenerative MRL/MpJ-like activity compared to either constituent alone. We addressed these goals by adopting an experimental approach integrating primary cell culture, functional *in vitro* assays, and *in vivo* histological analyses that capture physiological aspects of acute tendon healing and quantitative proteomics to profile the secretome. We hypothesized that harnessing biological cues derived from the local MRL/MpJ tendon environment through recombinant protein design would recapitulate the beneficial effects of administering these

MRL/MpJ constituents *in vitro.* Our findings shed insight into the cellular processes and candidate protein regulators that drive effective mammalian tendon healing across rodent species, establishing a novel biologics-based therapeutic strategy that also provides a promising platform for future mechanistic interrogation.

Results

MRL/MpJ tenocytes demonstrate greater intercellular communication, cytoskeletal organization, mechanosensitivity, and ECM deposition than B6 tenocytes

We have previously shown that culturing B6 tenocytes on MRL/MpJ dPECM-coated 2D substrates attained a dendritic morphology consisting of axon-like protrusions and decreased circularity(12). To ascertain whether these protrusions are reflective of MRL/MpJ tenocyte behavior, we analyzed the single-cell morphology of B6 and MRL/MpJ tenocytes cultured on collagen I-coated substrates using phalloidin staining (**Fig. 1A and B**). Compared with B6 tenocytes, a significantly greater proportion of MRL/MpJ tenocytes formed actin-rich protrusions (70.3% compared to 88.9% of all cells, $P = 0.034$; **Fig. 1C**). There were no differences in the number of protrusions formed on a per cell basis between B6 and MRL/MpJ tenocytes (data not shown), indicating that the significantly greater total protrusion length (total and normalized to cell spreading area; $P < 0.0001$ and 0.0029, respectively) observed in MRL/MpJ tenocytes (**Fig. 1C**) is due to longer cytoskeletal extensions. Importantly, these results confirm that our prior observations are characteristic of MRL/MpJ tenocyte morphology that may mediate long-distance cell-cell contacts and could be suggestive of increased mechanosensitivity. Additionally, MRL/MpJ tenocytes also showed significantly lower cell circularity ($P = 0.0001$) and greater spreading area ($P = 0.03$) and perimeter ($P < 0.0001$) (**Fig. 1D**), which corroborates our prior morphological observations in B6 tenocytes cultured on MRL/MpJ dPECM also as characteristic of MRL/MpJ cell behavior. We next investigated whether these intrinsic differences in the actin cytoskeleton serve as a physical mediator to enable MRL/MpJ tenocytes to better engage with changes to their surrounding microenvironment.

It is well established that the contractile actomyosin machinery is required to drive changes in cell shape, adhesion, and motility that regulate cell signaling and behavior (17). In particular, actin-based cellular protrusions facilitate cell migration and spreading and are closely coupled with the formation of focal adhesions (FAs) such as vinculin. Vinculin regulates the recruitment and disassembly of these FAs that link the actin cytoskeleton to the ECM and enable cells to sense and respond to environmental factors (e.g., activation of growth factor-mediated signaling pathways, mechanical cues) (18–21). Thus, we hypothesized that the protrusion networks that are characteristic of MRL/MpJ tenocytes enhance mechanosensitivity and cell migration. Indeed, MRL/MpJ tenocytes exhibited significantly greater FA number (1.77-fold higher, $P < 0.0001$) and area (1.6-fold higher, $P = 0.0012$) than that of B6 tenocytes when cultured on collagen I-coated substrates (**Fig. 1E**). However, when normalized to cell spreading area, FA area was not statistically different between B6 and MRL/MpJ cells (data not shown; $P = 0.22$), but FA number remained significantly higher in MRL/MpJ tenocytes ($P = 0.001$). Moreover, the average FA size was significantly greater in B6 tenocytes than MRL/MpJ tenocytes (1.16 ± 0.064 μm^2 compared to 0.96 ± 0.05 μm^2), indicating that these MRL/MpJ protrusions are stabilized by smaller nascent adhesions (20) (<1 μm diameter). These findings indicate that MRL/MpJ tenocytes undergo rapid and robust turnover of smaller FAs that better stabilize the actin cytoskeleton and its integrin-mediated mechanotransduction compared

148 to B6 tenocytes. Furthermore, 2D wound scratch assays (**Fig. 1F**) showed significantly
149 increased MRL/MpJ tenocyte numbers at the defect site compared to B6 tenocytes on
150 fibronectin-coated substrates ($P = 0.048$; **Fig. 1G**). Cell migration was not different on
151 collagen I-coated substrates ($P = 0.25$) despite comparable protrusion networks on both
152 collagen I and fibronectin (**Fig. 1H**), indicating that changes to other cell-ECM and/or
153 cell-cell interactions during an injury response likely play a more important role in
154 modulating 2D tenocyte migration.
155
156 Cytoskeletal tension-induced activation of Hippo pathway effectors and transcriptional
157 coactivators, Yes-associated protein (YAP) and WW domain-containing transcription
158 regulator protein 1 (TAZ), regulates cell mechanosensing and adhesion-mediated
159 signaling (22–25). To ascertain whether our observations of increased stress fiber, FA, and
160 cellular protrusion formation in MRL/MpJ tenocytes is indicative of a YAP-dependent
161 mechanosignaling program, we next evaluated the effects of inhibiting actin stabilization
162 and ROCK-mediated cell contractility on YAP nuclear translocation. We cultured B6 and
163 MRL/MpJ tenocytes at low density on collagen I-coated substrates with and without
164 Latrunculin A (inhibitor of actin polymerization), blebbistatin (inhibitor of myosin II, a
165 downstream effector of ROCK), and Y-27632 (inhibitor of ROCK) for 4 hours and stained
166 for YAP (**Fig. 1I**). As expected, YAP nuclear translocation was significantly greater in
167 MRL/MpJ tenocytes than B6 tenocytes (1.46-fold higher, $P < 0.0001$) treated with the
168 DMSO vehicle control (**Fig. 1J**). No correlations were found between YAP nuclear
169 translocation and single-cell morphological parameters. To account for baseline
170 differences in YAP nuclear translocation between B6 and MRL/MpJ tenocytes, we
171 subsequently normalized data relative to the DMSO control and compared the relative
172 changes in YAP nuclear translocation with pharmacological inhibition between mouse
173 strains (**Fig. 1K**). Unsurprisingly, disruption of the actin cytoskeleton with Latrunculin A
174 treatment resulted in YAP being predominantly localized in the cytoplasm with no
175 difference in relative YAP nuclear translocation between B6 and MRL/MpJ tenocytes (P
176 $= 0.22$), indicating that actin polymerization is required for nuclear transport of YAP.
177 Inhibition of myosin II with blebbistatin treatment significantly reduced relative YAP
178 nuclear translocation in MRL/MpJ tenocytes compared to B6 tenocytes ($P < 0.0001$) with
179 MRL/MpJ tenocytes having greater cytoplasmic retention of YAP. Similarly, inhibition of
180 ROCK with Y-27632 treatment reduced relative YAP nuclear translocation in MRL/MpJ
181 tenocytes compared to B6 tenocytes ($P = 0.058$). These data confirm that MRL/MpJ
182 tenocytes harbor enhanced mechanosignaling dependent on myosin II- and ROCK-
183 mediated contractility to facilitate YAP nuclear translocation.
184
185 We next extended our characterization of B6 and MRL/MpJ cell behavior to confluent
186 culture conditions that are more reflective of the dPECM environment during the
187 proliferative phase of acute tendon healing at 7 dpi *in vivo* (11). After 7 days of culture in
188 full-serum media to reach confluency (**Fig. 2A**), cytoskeletal and cell-deposited
189 fibronectin coherency/alignment (**Fig. 2B-D**) were significantly greater in MRL/MpJ
190 tenocytes than B6 tenocytes (both $P < 0.0001$), consistent with early improvements in
191 cellular and ECM organization seen at 7 dpi *in vivo* in MRL/MpJ tendons compared to B6
192 tendons (11). Remarkably, many MRL/MpJ nuclei also assembled into tightly-packed,
193 linear arrays along fibronectin tracks (yellow dashed line; **Fig. 2C**) that closely resembled
194 physiological tendon organization despite the absence of structural or mechanical cues
195 during culture. MRL/MpJ tenocytes also exhibited significantly greater ECM deposition
196 (1.46- and 1.29-fold higher for fibronectin and collagen I, respectively; $P < 0.0001$ for
197 both) and thickness ($P = 0.0021$ for fibronectin), cell number (1.50-fold higher, $P <$

198 0.0001), and expression of connexin-43 (Cx-43) gap junctions ($P = 0.0089$) compared to
199 B6 tenocytes (**Fig. 2E and F**). Moreover, the increasingly anisotropic and fibrillar
200 fibronectin network generated by MRL/MpJ tenocytes is consistent with ROCK- and
201 mechanosignaling-mediated (e.g., ITGB1, FAK) pathways being known to regulate
202 fibronectin assembly (26–29). Visually, fibronectin and Cx-43 gap junctions were more
203 uniformly distributed throughout neighboring MRL/MpJ tenocytes, whereas these were
204 limited to the periphery of B6 tenocytes suggestive of disrupted cell-ECM adhesion
205 (yellow arrowheads, **Fig. 2C**). However, it is not clear whether increased Cx-43 gap
206 junction formation is characteristic of MRL/MpJ tenocyte behavior or driven by changes
207 in cell density. To overcome this limitation, we next cultured cells for 3 days in full-serum
208 media to yield comparable densities. Cx-43 expression remained significantly higher in
209 MRL/MpJ tenocytes than B6 cells (1.32-fold higher, $P = 0.024$) and predominantly
210 localized at the tips of actin-based cellular protrusions at cell-cell contact sites (yellow
211 arrowheads, **Fig. 2G**). There were no differences in αSMA expression after 3 ($P = 0.6$)
212 and 7 (2.2% lower, $P = 0.14$) days of culture (**Fig. 2H**), indicating that increased
213 cytoskeletal organization of MRL/MpJ tenocytes at confluency is not primarily mediated
214 by myofibroblast activity. In short, our data demonstrate that enhanced cytoskeletal and
215 ECM alignment, ECM deposition, and intercellular communication are fundamental to
216 MRL/MpJ tenocyte behavior and likely contribute to improved structural healing
217 outcomes.
218
219 Given these cell-intrinsic differences in B6 and MRL/MpJ tenocyte morphology and
220 behavior, we next used quantitative proteomics to identify growth factors and cytokines
221 enriched in the MRL/MpJ tenocyte secretome.
222
223 **The MRL/MpJ tenocyte secretome contains distinct biological signatures to those of**
224 **B6 tenocytes regardless of loading modality**
225 We first comprehensively characterized soluble proteins in B6 and MRL/MpJ tenocyte
226 secretomes by profiling concentrated static and dynamic (i.e., cells conditioned under
227 cyclic stretch using the CellScale MCFX bioreactor system) conditioned media samples
228 for up to 640 and 200 protein targets, respectively, using Quantibody Mouse Cytokine
229 Arrays (**Fig. 3A**). Due to sample volume constraints using the MCFX bioreactor compared
230 to traditional culture flasks, quantitative proteomics of the dynamic secretome was
231 restricted to 200 targets. There were no differences in protein concentration (**Fig. S1A**) or
232 cell number at the time of conditioned media collection (data not shown) between B6 and
233 MRL/MpJ secretome samples. In the static secretome (**Fig. 3B**), we identified 336
234 cytokines of which 252 (75% of detected proteins) were differentially expressed proteins
235 (DEPs) between B6 (50.9% of detected proteins, 118 enriched in B6, 53 only detected in
236 B6) and MRL/MpJ tenocytes (24.1% of detected proteins, 74 enriched in MRL/MpJ, 7
237 only detected in MRL/MpJ). In the dynamic secretome (**Fig. 3B**), we identified 56
238 cytokines of which 43 (76.8% of detected proteins) were differentially expressed between
239 B6 (44.6% of detected proteins, 21 enriched in B6, 4 only detected in B6) and MRL/MpJ
240 tenocytes (32.1% of detected proteins, 17 enriched in MRL/MpJ, and 1 only detected in
241 MRL/MpJ). Of note, interleukin-3 (IL-3) was only detected in the B6 secretomes, tumor
242 necrosis factor alpha (TNF-α) was only detected in the dynamic secretomes, and TNF
243 receptor 2 (TNF RII), thymic stromal lymphopoietin (TLSP), and nephrilysin were only
244 detected in the static secretomes. We applied multivariate analyses using principal
245 components analysis (PCA; **Fig. 3C**) and found that B6 and MRL/MpJ static secretomes
246 formed separate clusters along PC1 (34.4% of total variance). PCA revealed minor
247 overlap of B6 and MRL/MpJ dynamic secretome samples reflective of higher biological

variation. Heatmap visualization corroborated these observations as evidenced by a greater degree of sample clustering in the static secretomes (**Fig. 3D**) compared to the dynamic secretomes (**Fig. 3E**). We performed Kyoto Encyclopedia of Genes and Genomes (KEGG) overrepresentation analysis of all static secretome DEPs using a dot plot and implicated several inflammatory pathways, including tumor necrosis factor (TNF), toll-like receptor (TLR), nuclear factor-kappa B (NF-κB), T and B cell receptor, interleukin, cytokine, and chemokine signaling (**Fig. S2A**). Supporting our YAP data in the present study, our IPA upstream regulator analysis found that Rho-associated protein kinase 1 (ROCK1) and other putative drivers of YAP activation (integrin beta-1; ITGB1, focal adhesion kinase; FAK, Ras-related C3 botulinum toxin substrate 1; Rac1) were predicted to be upregulated in the MRL/MpJ static secretome.

On the basis that tenocytes experience cyclic stretching due to dynamic tensile loading, we next conducted comparative analyses of the static and dynamic secretomes using IPA to determine canonical pathways, upstream regulators, and diseases and functions that are differentially regulated with mechanical stimulation. Surprisingly, mechanical stimulation had a minimal effect on the majority of diseases and functions (**Fig. 3F and Table S2**) and canonical pathways (**Fig. 3G**)—most of which are involved in inflammation and cell death—with similar Z-score activation patterns between the static and dynamic secretomes. In contrast, minimal agreement was found for upstream regulators with 8 of the top 10 annotations having contrasting activation states (**Fig. S1B**), suggesting molecular changes in B6 and MRL/MpJ tenocyte activity with mechanical stimulation that nonetheless lead to comparable cellular functions and outcomes. To assess the effects of mechanical stimulation on the secretion of soluble factors detected in both secretome datasets, we next compared the relative change in protein concentrations for 46 cytokines shared between the static and dynamic secretomes. Interestingly, we found that B6 and MRL/MpJ dynamic secretomes showed similar fold change expression for 37 cytokines (80.4% of total) compared to their respective static secretomes (**Fig. 3H**). Overall, these distinct paracrine signaling signatures between B6 and MRL/MpJ tenocytes regardless of loading modality illustrate further cell-intrinsic differences that distinguish scar-mediated and scarless tendon healing outcomes.

Adult quiescent MRL/MpJ tenocytes undergo greater proliferative and apoptotic activity compared to B6 tenocytes

Altered cell cycle control (e.g., elevated G2/M accumulation) has been proposed as a potential characteristic of the regenerative MRL/MpJ cell phenotype (7), leading us to next characterize the growth kinetics and endogenous β-Galactosidase (β-Gal) activity, a marker for cellular senescence (i.e., irreversible cell cycle arrest), between B6 and MRL/MpJ tenocytes (**Fig. 4A and B**). B6 tenocytes showed a significantly higher percentage of β-Gal-positive/senescent cells at passage four (45.4%, $P = 0.022$) and five (60.7%, $P < 0.0001$) compared to passage three (25.3%; **Fig 4C**). In contrast, MRL/MpJ tenocytes displayed minimal cellular senescence with no significant changes in β-Gal expression with increasing passage numbers (0.3%, 1%, and 6%; **Fig. 4C**). These results were accompanied by a progressive decline in B6 tenocyte population doubling time (PDT) with serially passaging, whereas MRL/MpJ tenocyte PDT remained constant and was significantly lower than that of B6 cells at passage four (1.99-fold lower, $P = 0.032$) (**Fig. 4D**). Although growth rates were comparable at earlier passages, cumulative population doubling (CPD) at passage four was significantly greater in MRL/MpJ tenocytes compared to B6 tenocytes (1.32-fold higher, $P = 0.0048$). At each passage, both the percentage ($P = 0.003$ at P3, < 0.0001 at P4, < 0.0001 at P5) and number of senescent

298 cells ($P = 0.018$ at P3, < 0.0001 at P4, < 0.0001 and P5; **Fig. S3A**) were significantly
299 higher in B6 tenocytes compared to MRL tenocytes. The total cell number was not
300 different between B6 and MRL/MpJ tenocytes (**Fig. S3B**). Collectively, these data
301 demonstrate that MRL/MpJ tenocytes are more resistant to replicative senescence and
302 exhibit superior expansion potential compared to B6 tenocytes. Given that growth arrest
303 and resistance to pro-apoptotic stimuli are hallmarks of cellular senescence (30,31), we
304 next performed immunohistochemical (IHC) analysis of Ki-67 and cleaved caspase-3,
305 markers of cell proliferation and apoptosis respectively, of injured B6 and MRL/MpJ
306 patellar tendons during the proliferative and remodeling phases of healing (**Fig. 4E**). As
307 expected, MRL/MpJ tendons had significantly increased cell proliferation (**Fig. 4F**) and
308 apoptosis (**Fig. 4G**) compared to B6 tendons at 1 wpi (Ki-67: $P < 0.0001$, caspase-3: $P =$
309 0.0032) and 4 wpi (Ki-67: $P = 0.0027$, caspase-3: $P = 0.029$), providing evidence that
310 corroborates the relevance of our *in vitro* findings as potentially conserved mechanisms at
311 play during the more complex *in vivo* healing environment.
312
313 The p53/p21 signaling axis is thought to play a critical role in MRL/MpJ tissue
314 regeneration wherein the absence of p21 promotes senescence, hyperproliferation, and the
315 DNA damage response (32). Notably, $p21^{-/-}$ knockout and MRL/MpJ mice are capable of
316 regenerating full-thickness ear and articular cartilage defects (32,33). To determine
317 whether reduced p21 expression and endogenous DNA damage are associated with
318 MRL/MpJ tenocyte behavior *in vitro*, we stained B6 and MRL/MpJ cells for endogenous
319 p21 and γH2AX. Contrary to reports of linking appendage regeneration to a lack of p21
320 expression in MRL/MpJ ear fibroblasts(32), we detected endogenous p21 activity in
321 MRL/MpJ tenocytes (**Fig. 4H**). There were no differences in the number of γH2AX-
322 positive foci that mark DNA double-stranded breaks (**Fig. S4A**) or p21 expression (**Fig.**
323 **S4B**), indicating that MRL/MpJ tenocyte quiescence and proliferation may be regulated
324 independently of p21 and DNA damage repair mechanisms.
325
326 After elucidating key biological processes underlying MRL/MpJ tenocyte behavior, we
327 interrogated the biochemical milieu of the local MRL/MpJ tendon environment by
328 culturing B6 and MRL/MpJ tenocytes using a combination of their dPECM-coated
329 substrates (12) and the secretome.
330
331 **B6 and MRL/MpJ tenocytes treated with MRL/MpJ-derived proteins attain**
332 **comparable single-cell morphology and cell-ECM interactions**
333 We have previously shown that dPECM harvested from MRL/MpJ tendon at 1 wpi
334 enhance B6 tenocyte cell morphology and proliferation *in vitro*. Additionally, comparative
335 analyses results in IPA showed similar biological annotations between the static and
336 dynamic secretomes, motivating the use of the static secretome in subsequent experiments
337 for practicality. Accordingly, we investigated three experimental conditions: (*i*) a scar-
338 mediated healing group of B6 tenocytes treated with B6-derived components (i.e., dPECM
339 and secretome) (referred to as 'BB'), (*ii*) a therapeutic group of B6 tenocytes treated with
340 MRL/MpJ-derived components (referred to as 'BM'), and (*iii*) a positive control group of
341 MRL/MpJ tenocytes treated with MRL/MpJ-derived components (referred to as 'MM').
342
343 Strikingly, B6 and MRL/MpJ tenocytes at a low cell density treated with MRL/MpJ-
344 derived components displayed identical single-cell morphology, FA formation, and
345 cellular protrusion patterns (**Fig. 5A and B**). In contrast, BB exhibited significantly higher
346 cell circularity and lower perimeter, number of FAs and total FA area, and protrusion
347 parameters (percentage of cells with protrusions, number of protrusions, total protrusion

348 length, total protrusion length normalized to cell perimeter) compared to BM and MM
349 (**Fig. 5D-F**). Additionally, B6 tenocytes treated with MRL/MpJ-derived components
350 exhibited significantly higher αSMA expression compared to B6 tenocytes treated with
351 B6-derived components ($P = 0.016$) or at baseline ($P < 0.0001$) (**Fig. 5G and H**),
352 suggesting that myofibroblast activity is transiently increased but does not remain elevated
353 with extended culture periods. Interestingly, B6-derived components elicited little or no
354 effect with BB being largely comparable to untreated B6 tenocytes. Supporting our
355 hypothesis, these findings demonstrate that MRL/MpJ-derived components reprogram cell
356 morphology and amplify mechanotransduction pathways towards MRL/MpJ tenocyte
357 behavior.
358
359 We next assessed the capacity of MRL/MpJ-derived components to enhance cytoskeletal
360 organization, ECM deposition, and Cx-43 formation in confluent B6 tenocytes (**Fig. 6A**).
361 To minimize the influence of serum proteins and confounding effects from differences in
362 total cell number due to increased MRL/MpJ tenocyte proliferation, cells were seeded at a
363 high density and subsequently maintained in low-serum media with or without exogenous
364 secretome supplementation. Moreover, to definitively ascertain whether there is a
365 combined benefit of administering the MRL/MpJ-derived components, we also cultured
366 B6 tenocytes with MRL/MpJ dPECM or secretome alone with cells cultured in only low-
367 serum media served as baseline controls. Consistent with our previous baseline B6 and
368 MRL/MpJ comparisons under culture in full-serum media, MRL/MpJ tenocytes showed
369 greater baseline F-actin alignment ($P = 0.0003$), fibronectin deposition (1.20-fold higher,
370 $P = 0.095$), collagen I deposition (1.15-fold higher, $P = 0.0029$), and no difference in
371 αSMA expression compared to B6 tenocytes (**Fig. 6B**). In contrast with our previous data
372 in full-serum media, MRL/MpJ tenocytes exhibited significantly lower baseline Cx-43
373 expression than B6 tenocytes under low-serum conditions (1.96-fold lower, $P < 0.0001$).
374 Supporting our hypothesis, B6 and MRL/MpJ tenocytes treated with MRL/MpJ-derived
375 components showed comparable F-actin alignment and relative changes in fibronectin
376 deposition that were significantly higher than that of B6 tenocytes treated with B6-derived
377 components (**Fig. 6C and D**). BM also showed greater collagen I deposition compared to
378 BB ($P = 0.10$) (**Fig. S6A**). Due to restricted ECM deposition under low-serum conditions,
379 fibronectin alignment could not be quantified. Contrary to our hypothesis, BB and BM had
380 comparable Cx-43 expression that were significantly lower than MM. However, these
381 discrepancies are largely attributed to a nearly two-fold reduction in Cx-43 expression in
382 MRL/MpJ at baseline, as evidenced by comparable staining profiles between cells that
383 received any combination of mouse-derived components. This data suggest that these
384 tenocytes upregulate Cx-43 expression in response to mitogenic stimulation. There were
385 no differences in αSMA expression between all treatment groups. Further supporting our
386 hypothesis, F-actin alignment and Cx-43 levels were significantly higher in B6 tenocytes
387 treated with MRL/MpJ-derived components compared to dPECM ($P = 0.0031$ for F-actin
388 and $P < 0.0001$ for Cx-43) or secretome ($P = 0.031$ for F-actin and $P = 0.002$ for Cx-43)
389 alone (**Fig. 6E**), confirming the combined benefit of administering the MRL/MpJ-derived
390 components.
391
392 Lastly, we determined whether MRL/MpJ-derived components could promote cell
393 proliferation and attenuate the onset of cellular senescence by treating B6 tenocytes
394 cultured at a moderate density for 3 days and staining for ß-gal activity (**Fig. 6F**). There
395 was no difference in cell number between B6 and MRL/MpJ tenocytes at baseline or
396 between cells treated with MRL/MpJ-derived components. Supporting our hypothesis,
397 compared with BB, BM showed significantly increased total cell number (1.17-fold

398 higher, $P = 0.045$). In addition, total cell number was significantly higher in B6 tenocytes
399 treated with MRL/MpJ-derived components compared to dPECM ($P = 0.036$) or
400 secretome ($P = 0.0002$) alone (**Fig. 6G**). These results are consistent with previous
401 observations that an early increase in tenocyte proliferation is a hallmark of MRL/MpJ
402 tendon healing(10,12). However, contrary to our hypothesis, there was no difference in the
403 number or percentage of senescent cells between BB and BM. B6 tenocytes treated with
404 only secretome exhibited less senescence overall compared to BM (1.15-fold lower, $P =$
405 0.074), but no differences were found in the number of senescent cells between all B6
406 tenocyte groups. Altogether, these findings demonstrate that MRL/MpJ-derived
407 components potently augment B6 tenocytes towards pro-regenerative MRL/MpJ-like
408 behavior despite the persistence of a senescent subpopulation of cells.
409
410 Collectively, our data provide compelling evidence that the combined administration of
411 MRL/MpJ-derived components modulates B6 tenocytes toward an MRL/MpJ-like cell
412 phenotype. However, there are important considerations in harnessing these biological
413 cues for therapeutic delivery. First, the tendon ECM and secretome each contain
414 thousands of biomolecules (34,35), which can preclude their feasibility to scale up for
415 preclinical testing in animal models. Second, it remains unclear whether these hallmarks
416 of MRL/MpJ tenocyte behavior and the therapeutic utility of MRL/MpJ-derived
417 components are conserved across other mammalian species. To address these points, we
418 sought to develop a panel of recombinant proteins using our quantitative proteomics
419 datasets. The final objective of this study was to assess the functional activity of B6-
420 derived components, MRL/MpJ-derived components, and the recombinant protein
421 therapeutic *in vitro* on patellar tenocytes derived from scar-mediated healing Sprague-
422 Dawley (SD) rats. We hypothesized that the recombinant protein therapeutic will
423 recapitulate the effects of the MRL/MpJ-derived components on rat tenocyte behavior *in*
424 *vitro* and that these changes will be consistent with our mouse data.
425
426 **Recombinant protein therapeutic promotes regenerative MRL/MpJ-like tenocyte**
427 **behavior across species**
428 Mouse and rat models closely recapitulate human tendon anatomy and physiology (36,37),
429 supporting the use of rodent tenocytes to investigate the proof-of-concept translational
430 capacity of our recombinant protein therapeutic. However, despite the prevalent use of
431 rodent models for tendon research, a comparative evaluation of baseline mouse and rat
432 tenocytes behavior is lacking. Accordingly, we first cultured B6 and SD patellar tenocytes
433 on collagen I-coated substrates and analyzed their single-cell morphology. There were no
434 differences in any morphological (cell circularity, spreading area, perimeter), cellular
435 protrusion parameters (percentage of cells with protrusions, number of protrusions, total
436 protrusion length), or αSMA expression between B6 and SD tenocytes (**Fig. S7A and B**)
437
438 A candidate panel of 29 recombinant proteins (10 structural and 19 soluble, 12 of which
439 were from the secretome) was identified from a systemic screen of our quantitative
440 proteomics data (**Table 1**). However, a preliminary set of 17 recombinant proteins
441 (indicated in bold) were employed in the present study for our protein therapeutic (**Fig.**
442 **7A**) due to several proteins being on backorder or lacking commercial availability at the
443 time of investigation. To mimic our combined dPECM and secretome culture system with
444 the recombinant protein therapeutic, structural proteins were sequentially adhered onto a
445 collagen I-coated substrate starting with acid-solubilized proteins followed by those
446 reconstituted in sterile 1X PBS. Soluble proteins were supplemented into low-serum
447 media. All protein concentrations used in this study were determined from published

reference values for *in vitro* administration. We then investigated three experimental conditions: (*i*) a scar-mediated healing group of SD tenocytes treated with B6-derived components (referred to as 'RB'), (*ii*) a positive control group of SD tenocytes treated with MRL/MpJ-derived components (referred to as 'RM'), and (*iii*) the therapeutic group of SD tenocytes treated with the recombinant protein therapeutic (referred to as 'RP'). For the B6-derived components, B6 uninjured dECM was used as the substrate coating instead of the dPECM to match the conditions analyzed via mass spectrometry in our published *in vivo* study (16).

Based on our results that cell morphology is preserved across B6 and SD tenocytes, we were able to definitively ascertain the effects of our recombinant protein therapeutic on SD tenocyte behavior. Compared with MRL/MpJ-derived components, the recombinant protein therapeutic increased the number of protrusions ($P = 0.0088$) and total protrusion length ($P = 0.09$, 0.041 when normalized to cell perimeter) (**Fig. 7B and C**). Additionally, there were no differences in the number of protrusions or total protrusion coverage (normalized to cell perimeter) between RB, RM, or baseline. As expected, SD tenocytes cultured with the recombinant protein therapeutic and MRL/MpJ-derived components exhibited comparable cell circularity, spreading area, and αSMA expression (**Fig. 7D**). Supporting our hypotheses, RM and RP exhibited significantly lower circularity and higher perimeter, spreading area, αSMA expression, percentage of cells with protrusions, and total protrusion length compared to RB. Taken together, these results establish that the morphological features of MRL/MpJ tenocyte can be achieved in SD tenocytes through the selective delivery of key proteins. Further supporting our hypotheses, SD tenocytes treated with the recombinant protein therapeutic and MRL/MpJ-derived components showed comparable F-actin alignment and were significantly higher than that of SD tenocytes treated with B6-derived components ($P < 0.0001$ for both) (**Fig. 7E and F**). Moreover, RP displayed significantly higher F-actin alignment compared to RM ($P = 0.02$). Contrary to our hypothesis, while the recombinant protein therapeutic ($P = 0.09$) and MRL/MpJ components ($P = 0.37$) increased fibronectin deposition compared to the baseline control, these changes were not statistically significant. However, this may potentially be attributed to the recombinant protein therapeutic only containing 17 out of the 29 identified candidates. Lastly, we found significantly lower total cell number in RP compared to RM (9.8% lower; $P = 0.04$), suggesting that the recombinant protein therapeutic induces apoptosis that leads to more effective cytoskeletal alignment consistent with increased cell turnover during MRL/MpJ scarless tendon healing *in vivo*.

Discussion

The widespread benefits of using tissue-specific dECM (38,39) and mesenchymal stem/progenitor cell-sourced secretome (35,40) to stimulate tissue repair and regeneration have been thoroughly established. However, there has been little exploration on the effects of these components together despite their capability to support complex cell-ECM and cell-cell interactions. Supporting the use of this combined biologic approach, our study integrated the structural constituents and cell-secreted soluble factors enriched in the MRL/MpJ tendon dPECM and secretome to modulate scar-mediated healing tenocytes towards an MRL/MpJ-like phenotype *in vitro*. These findings also provide mechanistic insight into the biological processes underlying regenerative MRL/MpJ tenocyte behavior and establish *in vitro* metrics grounded in physiologically relevant *in vivo* acute injury outcome measures. A major hurdle to harnessing the MRL/MpJ dPECM and secretome

498 for therapeutic applications is that they each contain thousands of biomolecules, most of
499 which may not be essential in delineating scar-mediated and regenerative healing, which
500 presents challenges in translating these components for larger animal testing. Accordingly,
501 our study isolated a panel of candidate protein regulators of mammalian tendon
502 regeneration that exerts interspecies utility by enhancing scar-mediated healing rat
503 tenocyte activity. Our data showed that rat tenocytes treated with the recombinant protein
504 therapeutic outperformed the MRL/MpJ-derived components as evidenced by increased
505 cellular protrusion formation and cytoskeletal alignment. These findings indicate that our
506 approach of selectively administering recombinant proteins is functionally advantageous,
507 which may be attributed to limiting unnecessary protein-protein interactions and instead
508 achieving more targeted modulation of the molecular processes and downstream effectors
509 that regulate MRL/MpJ cell behavior.
510
511 Constitutive stabilization of HIF-1α expression and p21 downregulation have both also
512 been shown to control ear wound regeneration in adult MRL/MpJ mice (7,41). In contrast,
513 multilineage differentiation, pluripotency markers, and HIF-1α expression were not
514 observed in this study. We also found no difference in p21 expression between B6 and
515 MRL/MpJ tenocytes consistent with findings reported by Lalley *et al* (10). Therefore, our
516 data implicate resident tenocyte or progenitor cell populations as key mediators of
517 MRL/MpJ tendon healing outcomes. Supporting our proposed paradigm, Grinstein *et al*.
518 (42) recently identified a latent population of *Axin2*$^{+}$ tenocytes in the midsubstance of
519 mouse and human tendons that is recruited to the injury site, proliferate, and transiently
520 adopt injury responsive states to centrally organize the healing response. Our results
521 illustrated that rodent tenocytes treated with MRL/MpJ-derived components or our
522 recombinant protein therapeutic are robustly reprogrammed *in vitro* to attain
523 morphological characteristics identical to those of MRL/MpJ tenocytes. This
524 observation generates an exciting direction for future studies to determine whether adult
525 scar-mediated healing tenocytes retain a pro-regenerative capacity that is activated upon
526 exposure to therapeutic interventions *in vivo*.
527
528 Although healthy tenocytes were collected from young adult animals in this study, a
529 quarter of B6 tenocytes expressed senescent ß-gal activity whereas MRL/MpJ tenocytes
530 maintained a minimally senescent phenotype. Some studies have causally related TSDC
531 and tenocyte senescence to pathological aging and chronic degenerative tendinopathy,
532 whereby their accumulation leads to diminished tenogenic differentiation and cytoskeletal
533 organization, reduced cell migration, upregulation of proinflammatory signaling cascades,
534 and aberrant ECM remodeling (43–46). These changes extended to B6 tenocytes in our
535 data when comparatively evaluating baseline B6 and MRL/MpJ tenocyte behavior *in*
536 *vitro*. Similarly, Kallenbach and Freeberg *et al*. recently reported downregulated
537 senescence-associated pathways in MRL/MpJ flexor tendon healing compared to that of
538 B6 using bulk transcriptomic analyses (14). However, to our surprise and contrary to our
539 ß-gal staining data, the static secretome of MRL/MpJ tenocytes was enriched for more
540 known human senescence-associated secretory phenotype (SASP) factors (47) compared
541 to that of B6 tenocytes, suggesting a potentially beneficial and tissue-dependent context
542 for some of these SASP factors. Mounting evidence has shown that other regenerative
543 animal models such as zebrafish and amphibians undergo tissue damage-induced cellular
544 senescence that is localized to the injury site (48,49). Additionally, genetic or
545 pharmacological (e.g., senolytic and senomorphic agents) removal of senescent cells *in*
546 *vivo* has resulted in both reparative and impaired healing outcomes (49–51), underscoring
547 divergent roles of developmentally- and injury-induced cellular senescence during wound

healing. Considering that MRL/MpJ-derived components shifted B6 tenocytes towards a pro-regenerative phenotype without affecting the number of senescent cells, we speculate that these MRL/MpJ-enriched proteins overcome the degenerative ECM response associated with senescence and maintain some degree of phenotypic reprogramming even on senescent cells, as evidenced by consistent changes to their single-cell morphology. Future work should determine the extent to which these senescent tenocytes react to treatment by examining single-cell parameters in ß-gal-positive tenocytes via multiplexed IF staining.

Our findings establish that the enhanced cell contractility that defines the MRL/MpJ tenocyte phenotype are stabilized by the formation of cellular protrusions and focal adhesions. Scar-mediated rodent tenocytes treated with MRL/MpJ-derived components or our recombinant protein therapeutic not only mimicked these cellular features but also activated a more contractile myofibroblastic phenotype. Relatedly, Alisafaei *et al*. (52) recently discovered a positive two-way feedback loop between cellular protrusion dynamics and local ECM and mechanical anisotropy that promote fibroblastic activation and effective collagen remodeling. Moreover, we and others (53) have shown that connexin-43 localizes along tenocyte processes before assembling into cell-cell gap junctions at higher cell densities. Connexin-43 is the most abundant gap junction present in adult tendons, forming longitudinal and lateral contacts that regulate cellular metabolism, mechanosensitivity (e.g., stretch-induced calcium and ATP release), and intercellular communication through paracrine and autocrine effects (54–56). Taken together, these results suggest that early upregulation of connexin-43 activity through mitogenic stimulation with MRL/MpJ-derived components or the recombinant protein therapeutic facilitates an expedited healing response characterized by increased tenocyte proliferation, migration, and fibronectin deposition. Fibronectin is key constituent of the provisional ECM that guides cell adhesion, collagen assembly and fibrillogenesis, and temporal sequestration and release of soluble factors to further modulate cell behavior (57,58). Aberrant fibronectin accumulation is associated with long-term myofibroblast survival and persistence that ultimately drives scar-mediated tendon healing (59–61). In the context of the proliferative phase of acute tendon healing, our *in vitro* data suggest that MRL/MpJ tenocytes rapidly proliferate and undergo transient increases in αSMA expression and cell contractility, which self-regulates their cytoskeletal organization to enable early deposition of highly aligned fibronectin networks that promote cell migration and remodeling activity. Supporting these proposed cellular mechanisms, cell proliferation and apoptosis remained significantly elevated in MRL/MpJ tendons compared to B6 tendons at 1 and 4 wpi following acute injury *in vivo* in the present study. This data indicates a high turnover capacity of the MRL/MpJ tendon environment in actively recruiting cells throughout the proliferative and remodeling phases of healing to resolve the injury site while simultaneously preventing excessive ECM deposition that leads to scar formation. Overall, these findings shed light into the biological mechanisms that can inform the development of therapeutics for mammalian tendon regeneration.

This study is not without some limitations. First, the tendon sheath was excluded when isolating primary tendon cells as established by Bi *et al* (62). As this study also did not assess the presence of TSPCs *in vivo*, the precise functional contributions of sheath-derived TSPCs in MRL/MpJ tendon regeneration remain to be elucidated. Second, Quantibody-based proteomics are limited to preselected cytokine targets, are unable to distinguish between latent and active forms (e.g., matrix metalloproteinases; MMPs), and typically cannot recognize pro-peptides and membrane-bound cytokines (e.g., activin,

598 IGF, TGFß). Despite these concerns, Quantibody assays offer pg-level sensitivity greater
599 than that of traditional liquid chromatography-mass spectrometry (LC-MS) techniques
600 (63) and thus allow for the quantitative detection of rare and low-abundance soluble
601 proteins that are capable of engaging in ligand-receptor signaling. However, LC-MS
602 technologies remain the analytical standard for deciphering a wide range of large intact
603 proteins that comprise the ECM composition. Third, our study only analyzed male animals
604 for generating primary cell lines, dPECM, and secretome as well as functional assays. We
605 have recently shown that adult male and female MRL/MpJ tendons both demonstrate a
606 regenerative capacity with vastly improved mechanical recovery compared to those of B6
607 mice (13). More recently, we also found that both male and female MRL/MpJ tenocytes
608 exhibit similar or superior *in vitro* outcome measures, as detailed in the present study,
609 compared to B6 tenocytes (64). These findings suggest that the cellular and molecular
610 mechanisms underlying MRL/MpJ tendon regeneration are largely conserved between
611 sexes. Future experiments should further investigate the extent of sexual dimorphism in
612 MRL/MpJ tendon regeneration and ensure that the recombinant protein therapeutic
613 similarly modulates female rodent tenocytes towards an MRL/MpJ-like phenotype.
614
615 There are several technical and scientific considerations in moving towards *in vivo*
616 delivery of this recombinant protein therapeutic into clinically relevant tendon injuries in
617 larger animal models. First, the present study only evaluated a subset of 17 out of the 29
618 proteins identified from the quantitative proteomic analyses of the tendon ECM and
619 secretome. We anticipate that the incorporation of the remaining 12 proteins will amplify
620 the observed therapeutic effects on scar-mediated tenocytes (e.g., ECM deposition). The
621 integration of these proteins and their different molecular weights, isoelectric points, and
622 half-life properties is non-trivial from a drug delivery perspective. Furthermore, as not all
623 29 recombinant proteins may be necessary to achieve therapeutic efficacy *in vivo,* other
624 ongoing efforts will further refine this panel and assess its efficacy in tendon healing in
625 both acute and chronic overuse injuries. Recent studies have demonstrated that functional
626 blockade of molecular targets elevated during scar-mediated healing using neutralizing
627 antibodies *in vivo* ameliorated overuse-induced tendinopathy in mice (65). While our
628 study focused on evaluating the factors enriched in the MRL/MpJ tendon biological
629 environment, it should be noted that more than half of all cytokines in the static secretome
630 were increased or exclusively secreted by B6 tenocytes. Future studies will interrogate
631 whether the inhibition of B6-enriched soluble factors can further augment the therapeutic
632 potential of our MRL/MpJ-informed protein therapeutic.
633
634 We have previously demonstrated that MRL/MpJ tendons retain their improved healing
635 capacity compared to B6 tendons when isolated from the systemic environment during *ex*
636 *vivo* organ culture (12). In addition, we and other groups have shown reduced macrophage
637 infiltration (10) and attenuated inflammatory pathways (11,13,14) in MRL/MpJ tendons
638 compared to B6 tendons during the proliferative phase of healing. These observations
639 motivated our overarching hypothesis that the local tissue environment is the primary
640 driver of MRL/MpJ tendon regeneration. Interestingly, the top four soluble proteins
641 enriched in the MRL/MpJ static secretome that were evaluated in this study – CXCL5
642 (LIX), CXCL1 (KC), macrophage inflammatory protein 2 (MIP-2), and semamorphin-3F
643 (SEMA3F) – are chemokines and cytokines known to be potent mediators of early
644 neutrophil recruitment and retainment (66–70). In contrast, decreased circulating serum
645 levels of LIX, KC, MIP-2α during acute tendon injury have been attributed to the
646 regeneration of MRL/MpJ ear wounds (68) and tendons (14). Therefore, we postulate that
647 altered crosstalk between tenocytes and tissue-resident immune cells (e.g., macrophages)

648 or locally directed molecular cues may prompt neutrophils to initiate MRL/MpJ tendon
649 healing by concurrently streamlining the clearance of damaged tissue and the production
650 of the provisional ECM. Nonetheless, future studies should resolve the temporal
651 progression of the inflammatory cascade in MRL/MpJ tendon regeneration and assess the
652 potential immunomodulatory effects of the recombinant protein therapeutic *in vivo*.
653 Lastly, our study identified dual-specificity phosphatase 1 (DUSP1) as the most activated
654 upstream regulator in the B6 static secretome. DUSP1 is capable of dephosphorylating
655 major cell signaling pathways involved in innate immunity, cellular metabolism, and ECM
656 remodeling, including extracellular-signal regulated kinase (ERK) 1/2, mitogen-activated
657 protein kinase (MAPK), and c-Jun N-terminal kinase (JNK) (71–73). Conversely,
658 upstream analysis of the MRL/MpJ static secretome revealed activation of ERK, p38
659 MAPK, and Jun, thus suggesting that these pathways may be upregulated in MRL/MpJ
660 tendon regeneration and could be the basis for future mechanistic interrogation.
661
662 In summary, we demonstrate that the biological mechanisms underlying MRL/MpJ
663 tenocyte behavior can be induced across different mammalian species using a subset of
664 recombinant proteins, which may ultimately have transformative impact for promoting
665 tendon regeneration.
666
667 **Materials and Methods**
668 **Experimental Design**
669 The objective of this study was to assess the utility of MRL/MpJ tendon ECM- and
670 secretome-derived proteins in promoting regenerative outcomes across different species of
671 tenocytes. First, we identified cellular and biological processes that delineate scar-
672 mediated B6 and regenerative MRL/MpJ tenocyte behavior using primary cell culture
673 assays and confocal microscopy. Next, we demonstrated that the combined administration
674 of secretome and decellularized provisional ECM (dPECM) obtained from healthy
675 MRL/MpJ cells and hole-punched tendons at 7 dpi, respectively, modulates B6 cells
676 toward an MRL/MpJ-like phenotype *in vitro*. Lastly, we identified key constituents
677 enriched in the MRL/MpJ secretome using quantitative proteomics and subsequently
678 evaluated the functional activity of a panel of structural and soluble recombinant proteins
679 on rat tenocytes *in vitro*. We hypothesized that selectively delivering this panel of
680 recombinant proteins will recapitulate the effects of the MRL/MpJ-derived components on
681 tenocyte behavior. We further hypothesized that this therapeutic will elicit interspecies
682 utility as a novel therapeutic strategy for tendon healing. All experiments were carried out
683 at passage three (mouse) or passage four (rat) with a minimum of three biological
684 replicates (*N*) unless specified otherwise. For each biological replicate, three technical
685 replicates (*n*) were included.
686
687 **Animals and patellar tendon midsubstance punch injury**
688 All animal procedures were approved by the Cornell University Institutional Animal Care
689 and Use Committee (IACUC). Male 16- to 18-week-old B6 and MRL/MpJ mice were
690 bred in-house with the original dame and sire purchased from The Jackson Laboratory (B6
691 #000664 and MRL/MpJ #000486), unless specified otherwise, with five animals housed
692 per cage. Male 9- to 10-month-old SD rats were purchased from Envigo (#002) with two
693 animals housed per cage. Animals were maintained under alternating 12-hour light/dark
694 cycles with ad libitum access to food and water.
695
696 To generate tendon dPECM, a full-thickness midsubstance injury was introduced into the
697 left patellar tendon of male B6 and MRL/MpJ mice as described previously(12). Briefly,

698 mice were anesthetized with isoflurane (2% volume, 0.3 L/min) and received an
699 intraperitoneal administration of buprenorphine (1 mg/kg body weight). The fur was then
700 completely removed from the left leg before exposing the patellar tendon through a skin
701 incision above the knee cavity. A custom-machined stainless-steel backing (1.5-mm
702 width, 0.5-mm thickness) coated with a polyurethane adhesive (#1867T2; McMaster-Carr)
703 was inserted beneath the tendon before excising the tissue using a 1-mm biopsy punch.
704 After the backing was removed, the skin incision was closed using 6-0 Prolene sutures
705 (#8695G; Ethicon Inc.). Mice resumed cage activity and were euthanized after 1 wpi by
706 CO_2 administration followed by cervical dislocation. The provisional and contralateral
707 tendons were immediately harvested, snap-frozen in liquid nitrogen, and stored at -80°C
708 until use.
709
710 **Primary cell culture and reagents**
711 Low-glucose Dulbecco's modified Eagle's medium (#10-014; Corning) and lot-selected
712 fetal bovine serum (FBS; #35-015-CV; Corning) were used for primary cell expansion and
713 all experiments. Mouse cells were harvested from the patellar tendons of B6 and
714 MRL/MpJ mice as described previously(12). The tendon sheath and fat pad were removed
715 before enzymatic digestion with a mixture of collagenase type I (2 mg/mL) and
716 collagenase type IV (1 mg/mL) in serum-free media for up to 2 hours at 37°C on a rocking
717 shaker. To isolate primary tenocytes, tissue digests were passed through a 70-µm strainer.
718 Rat cells were similarly harvested from the patellar tendons of SD rats as described above
719 except the sheath remained intact. Independent cell isolation batches consisted of patellar
720 tendons pooled from five mice or one rat and served as biological replicates.
721
722 Cells were cultured in DMEM supplemented with 10% FBS and 1% antibiotics-
723 antimycotics (penicillin-streptomycin-amphotericin B; PSA; Gibco) (full-serum media) at
724 37°C and 5% CO_2 with media replenished every 2 days. Cells were routinely passaged at
725 80-90% confluency. For 2D ECM substrates, rat tail collagen I (#A1048301; Thermo
726 Fisher Scientific) and human plasma fibronectin (#33-016-015; Thermo Fisher Scientific)
727 were used. All cell lines employed in this study tested negative for mycoplasma
728 contamination (#LT07-703; Lonza).
729
730 **Immunofluorescence staining and confocal microscopy of cultured tenocytes**
731 For all immunofluorescence experiments, cells were cultured in glass-bottom 96-well
732 plates (#655892; Greiner Bio-One). Antibody details are available in the Supplementary
733 Materials (**Table S1**). Cells were fixed with 2% paraformaldehyde (PFA) for 10 minutes,
734 4% PFA for 20 minutes, washed thrice with 1X PBS, permeabilized with 0.1% Triton X-
735 100 for 15 minutes, and blocked with 3% bovine serum albumin (BSA; in 1X PBS) for 1
736 hour. Primary antibodies (in 3% BSA) were incubated overnight at 4°C unless specified
737 otherwise. Cells were then washed thrice with 1X PBS before incubating with secondary
738 antibodies (in 3% BSA) for 1 hour at room temperature in the dark. Lastly, cells were
739 washed thrice with 1X PBS, counterstained with DAPI (1:1000 dilution in 1X PBS;
740 #D1306; Thermo Fisher Scientific) for 30 minutes, and finally rinsed twice with 1X PBS
741 before imaging. For ECM staining, primary antibodies for fibronectin and collagen I were
742 incubated prior to permeabilization as to only label cell-deposited ECM.
743
744 Images were acquired using a Zeiss LSM710 confocal microscope (Zeiss) using a 25X
745 magnification water-immersion objective. Identical acquisition parameters were used
746 across samples for each independent experiment. All image analyses were conducted in
747 ImageJ (National Institutes of Health) by a blinded user.

748
749 **Tendon decellularization and preparation of dPECM coatings**
750 Tendons harvested from B6 and MRL mice were decellularized using a detergent-free
751 protocol inside a biosafety cabinet (BSC) as described previously (12,74). Briefly, the
752 tissues were incubated with 50 nM of Latrunculin B (#2182-1; BioVision) in DMEM for 2
753 hours at 37°C at 450 RPM to depolymerize actin networks. All subsequent incubation
754 steps were supplemented with 1X protease inhibitor cocktail (#78425; Thermo Fisher
755 Scientific) and conducted at room temperature at 450 RPM to minimize proteolysis. The
756 tissues were washed with deionized water for 30 minutes after Latrunculin B and
757 hypertonic incubation steps. After exposure to Latrunculin B, the tissues were incubated in
758 0.6 M KCl for 2 hours, 1.0 M KI for 2 hours, and then washed in DI water for 12 hours
759 followed by repeated KCl and KI incubation steps to induce osmolysis. Lastly, the tissues
760 were subsequently incubated in 1X phosphate-buffered saline (PBS) containing 1 kU/mL
761 of Pierce™ Universal Nuclease (#88702; Thermo Fisher Scientific) for 2 hours followed
762 by two consecutive 24-hour 1X PBS wash steps to clear residual cellular debris.
763 Decellularized tissues were lyophilized for 72 hours before being snap-frozen,
764 mechanically homogenized (Bread Ruptor 24, Omni, Inc.) using 2.8-mm ceramic beads
765 (#19-646; Omni, Inc.), solubilized (10 mg dry weight/mL) in 1 mg/mL pepsin (#P7012; in
766 0.1 M HCl; Sigma-Aldrich) for 72 hours at 4°C at 150 RPM, and stored at -80°C until use.
767 Flat-bottom 96-well plates were coated with solubilized dPECM (1 mg dry weight/mL
768 diluted in 0.1 M AcOH) overnight at 4°C. Coatings were washed twice with 1X PBS
769 immediately before use to remove residual acid.
770
771 To assess the contributions of the MRL/MpJ-derived components in modulating B6 cells
772 toward an MRL/MpJ-like phenotype, the following experimental groups were evaluated
773 for single-cell morphology and confluent mouse cell experiments: (1) B6 or MRL/MpJ
774 cells alone, (2) cells cultured with only dPECM, (3) cells cultured with only secretome,
775 and (4) cells cultured with both dPECM and secretome. MRL/MpJ cells treated with
776 MRL/MpJ-derived components served as a positive control.
777
778 **Secretome preparation and quantitative proteomics**
779 To generate the static secretome, B6 and MRL/MpJ cells were seeded at 90% confluency
780 on Nunc™ EasYFlask™ culture flasks (#159910; Thermo Fisher Scientific), rinsed once
781 with 1X DPBS (#21-030-CV; Corning), and subsequently incubated with phenol red-free,
782 serum-free media (#11054020, Thermo Fisher Scientific) supplemented with 2X
783 GlutaMAX™ (#35050061; Thermo Fisher Scientific) for 24 hours. The conditioned
784 medium was then collected, concentrated using ultrafiltration centrifugal devices (#88526;
785 3 kDa molecular weight cutoff; polyethersulfone membrane; Thermo Fisher Scientific),
786 and stored at -80°C until use.
787
788 To investigate the effect of mechanical stimulation on the secretome composition, silicone
789 well plates designed for the CellScale MCFX bioreactor (CellScale Biomaterials Testing)
790 were functionalized by surface silanization as described previously (75,76). Briefly,
791 silicone plates were plasma treated for 5 minutes followed by incubation with 10% (3-
792 aminopropyl)triethoxysilane (APTES; #440140; Sigma-Aldrich) in ethanol at 60°C for 60
793 minutes. The plates were then washed thrice with 1X PBS (#21-040; Corning), incubated
794 with 3% glutaraldehyde (#16539-60; Electron Microscopy Sciences) for 20 minutes at
795 room temperature, and rinsed twice with 1X DPBS before covalently coating the
796 substrates with provisional B6 and MRL/MpJ dPECM (1 mg/mL) overnight at 4°C. B6
797 and MRL/MpJ cells were seeded onto their respective dPECM-coated plates in full-serum

798 media and allowed to adhere for 12 hours to reach 90% confluency. To generate the
799 dynamic secretome, cells were then rinsed once with 1X PBS, incubated with serum-free
800 media supplemented with 2X GlutaMAX™, and immediately subjected to a homeostatic
801 uniaxial cyclic stretch regimen (4% sinusoidal strain at 1 Hz; additional details available
802 in Supplementary Materials) for 24 hours before collecting and concentrating the
803 conditioned medium as described above. Streptomycin is known to block stretch-activated
804 ion channels (77), so cells used for dynamic secretome collection were cultured in
805 medium without PSA.
806
807 Secretome was diluted to a 2X final working concentration for all *in vitro* experiments,
808 which was determined as the optimal concentration for promoting B6 tenocyte
809 proliferation (data not shown), in DMEM supplemented with 1% FBS and 1% PSA (low-
810 serum media) to limit the effect of high-abundance serum proteins. Secretome-containing
811 media was replenished every two days from the same batch to ensure consistency between
812 biological replicates. For quantitative proteomics ($N = 3$ per group), conditioned media
813 was normalized to total protein concentration as determined using the bicinchoninic acid
814 (BCA) assay (#23225; Thermo Fisher Scientific) and outsourced to RayBiotech to analyze
815 the cytokine concentrations of the static (Quantibody® Mouse Cytokine Array Q640; up to
816 640 targets) and dynamic secretomes (Quantibody® Mouse Cytokine Array Q4000; up to
817 200 targets). Secretome samples were processed and analyzed in the same batch for each
818 loading condition to minimize variation.
819
820 **Secretome proteomics bioinformatic analyses and visualization**
821 Any detected cytokines that were not within 75% of the lower limit of detection (LOD) of
822 the array were omitted from subsequent analyses. Cytokines with at least two uniquely
823 detected samples that were $\geq$ 1.2-fold change or only detected in one genotype were
824 regarded as differentially expressed proteins (DEPs). No comparisons for cytokines shared
825 between the static and dynamic secretomes were conducted as these conditions were
826 analyzed using different array technologies. Hierarchical cluster analysis was performed
827 using the online ClustVis (78) web tool to generate heatmap expression patterns of Z-
828 score normalized protein data for the static and dynamic secretomes. Differences between
829 secretome conditions were visualized by clustering biological replicates using
830 unsupervised principal components analysis (PCA). Canonical pathways, upstream
831 regulators, and disease and functions ($P \leq 0.05$ and $|$ Z-score $| \geq 1.5$) were performed using
832 Ingenuity Pathway Analysis (IPA; Qiagen). Positive and negative Z-score values indicate
833 predicted activation and inhibition, respectively, of biological functions determined by
834 IPA. For comparative analyses in IPA, a fold change of 2.0 was assigned as a placeholder
835 value to cytokines that were only detected in one genotype. Functional annotation of
836 KEGG pathway enrichment analyses and GO terms were performed in R and DAVID,
837 respectively.
838
839 **Immunohistochemical analysis of cell proliferation and apoptosis in B6 and**
840 **MRL/MpJ acute tendon injuries**
841 Male 12- to 13-week-old B6 and MRL/MpJ mice were purchased from The Jackson
842 Laboratory and underwent a 0.75-mm full-thickness midsubstance injury. Mice were
843 euthanized after 1 and 4 wpi to harvest the provisional tendons. Contralateral patellar
844 tendons harvested at 24-hours post-injury from a separate study were used as naïve
845 uninjured controls. Tendons were fixed in zinc formalin (#5701ZF, Thermo Fisher
846 Scientific), embedded in paraffin, and sectioned coronally at a thickness of 6 μm. All
847 subsequent immunohistochemical staining and image analysis were performed at the

848 midsubstance injury site by a blinded user. To measure cell proliferation and apoptosis,
849 sections were stained for cleaved caspase 3 and Ki-67, counterstained with toluidine blue,
850 and then imaged and stitched (Zeiss AxioVision; Oberkochen, Germany) at 20X
851 magnification. The number of positive and total cells were counted at the injury site in
852 ImageJ to calculate the percentage of apoptotic cells (*N* = 6-9 per group). Sections were
853 also stained for fibronectin using a custom MATLAB code to quantify the percentage of
854 positively-stained matrix (*N* = 6-9 per group) taken at 5X magnification.
855
856 **Cell senescence and population growth assays**
857 To evaluate the effect of serial passaging on cell growth, B6 and MRL/MpJ cells were
858 continuously cultured from P2-P4 (*N* = 5 per group averaged from n = 3 technical
859 replicates per *N*) and counted using a hemocytometer to calculate population doubling
860 level (PDL; **Equation 1**) and population doubling time (PDT; **Equation 2**):
861

$$PDL = PDL_0 + 3.322(\log \frac{N_f}{N_i}) \quad (1)$$

862

$$PDT = T * \frac{\log(2)}{\log(\frac{Nf}{N0})} \quad (2)$$

863
864 Where N_f is the cell number at the time of passage, N_i is the initial cell number seeded into
865 the flask, PDL_0 is the population doubling level of the previous passage, and T is the
866 culture period in hours. B6 and MRL/MpJ cells were then seeded at P3-P5 (5,000
867 cells/well) onto uncoated substrates in full-serum media and allowed to adhere for 24
868 hours. Cells were stained for β-galactosidase (β-Gal) as a marker of senescence using a
869 commercial kit (#9860S; Cell Signaling Technology) and imaged under an inverted
870 brightfield microscope at 10X magnification. The percentage of senescent cells (*N* = 5 per
871 group averaged from n = 3 technical replicates per *N*) was quantified at P3-P5 by counting
872 the number β-gal-positive and total cells. Static secretome DEPs were mapped onto a
873 published human SASP proteomic atlas(47) to correlate cellular senescence to biological
874 function.
875
876 To investigate the role of the dPECM and secretome in regulating cell senescence and
877 proliferation, B6 and MRL/MpJ cells were seeded (5,000 cells/well) onto uncoated or
878 dPECM-coated substrates in full-serum media and allowed to adhere for 24 hours. Cells
879 were then cultured in either low-serum or secretome-containing media for 3 days and
880 analyzed for β-Gal staining (*N* = 5 per group averaged from n = 3 technical replicates per
881 *N*) as described above.
882
883 **Immunofluorescence staining for p21 and DNA damage**
884 To measure p21 activity and intrinsic DNA damage, B6 and MRL/MpJ tenocytes were
885 seeded in full-serum media at a moderate density (5,000 cells/well) on uncoated substrates
886 and allowed to adhere for 24 hours. Cells were then washed once with 1X DPBS and
887 subsequently cultured in low-serum media for 24 hours prior to staining for p21 and
888 γH2AX. The nuclear p21 integrated density was averaged for all cells in each
889 representative image (*N* = 3 and *n* = 24 images per group). For γH2AX, the number of
890 positive foci (*N* = 3 and *n* = 215-216 cells per group) and pan-nuclear integrated density
891 were measured. (*N* = 3 and *n* = 24 images per group).
892
893 **Pharmacological inhibition of cytoskeletal tension and organization**

894 B6 and MRL/MpJ cells were seeded (750 cells/well) onto collagen I-coated (50 μg/mL)
895 substrates in full-serum media and allowed to adhere for 24 hours. To modulate
896 cytoskeletal tension, cells were treated for 4 hours with inhibitors against myosin II
897 (blebbistatin at 50 μM in DMSO; #B0560; Sigma-Aldrich), ROCK (Y-27632 at 50 μM in
898 DMSO; #1254; Tocris Bioscience), and actin polymerization (Latrunculin A at 0.5 μM in
899 DMSO; #10010630; Cayman Chemical Company). Cells treated with 0.1% DMSO served
900 as controls.
901
902 To assess differences in B6 and MRL/MpJ cell mechanotransduction and morphology,
903 cells were stained for the YAP and F-actin. YAP nuclear localization (nuclear-to-
904 cytoplasmic mean intensity ratio) and single-cell morphology (circularity; **Equation 3**,
905 perimeter, area, and F-actin integrated density) were thresholded and quantified (*n* = 72
906 cells per group, 8 cells per well).
907

$$Circularity = 4\pi * \frac{Area}{Perimeter^2} \quad (3)$$

908
909 **Cell migration assay**
910 For 2D cell migration experiments (*N* = 5 per group averaged from n = 3 technical
911 replicates per *N*), 96-well plates were coated overnight at 4°C with collagen I (50 μg/mL;
912 #A1048301; Thermo Fischer Scientific) or fibronectin (50 μg/mL; #33-016-015; Thermo
913 Fisher Scientific) to recapitulate biochemical cues associated with homeostasis and wound
914 healing, respectively. B6 and MRL/MpJ cells were seeded (7,500 cells/well) onto collagen
915 I- and fibronectin-coated substrates in full-serum media and allowed to adhere for 12
916 hours. Cells were serum starved in low-serum media for 18 hours to induce cell cycle
917 synchronization, manually scratched using a 200 μL pipette tip, rinsed once with 1X
918 DPBS, and subsequently cultured in low-serum media.
919
920 Transmitted light images were taken using a SpectraMax i3x Multi-Mode Microplate
921 Reader (Molecular Devices). The number of cells that migrated into the defect region was
922 quantified for 0- and 12-hours post-wounding.
923
924 **Modulating single-cell morphology, cytoskeletal protrusions, and focal adhesions**
925 To assess whether MRL/MpJ components are capable of shifting B6 cell morphology
926 toward previous observations(12) of decreased cell circularity and enhanced cytoskeletal
927 protrusions, B6 and MRL/MpJ cells were seeded (750 cells/well) onto collagen I- or
928 dPECM-coated substrates in full-serum media and allowed to adhere for 18 hours. Cells
929 were serum starved in low-serum media for 24 hours and cultured in either low-serum or
930 secretome-containing media for 24 hours. To assess differences in cell morphology and
931 focal adhesion formation, cells were stained for F-actin and vinculin, respectively.
932
933 Single-cell morphology was thresholded and quantified. Cytoskeletal protrusion metrics
934 (total number of protrusions, maximum protrusion length, total protrusion length) were
935 manually measured using the freehand line tool for all protrusions greater than 25 μm in
936 length. Semi-automated quantification of focal adhesions (total number of focal adhesions,
937 average focal adhesion area, number of focal adhesions normalized to cell area) was
938 performed as described previously (79). All experiments were analyzed with *N* = 3 per
939 group and up to *n* = 54 cells per group with an equal number of cells randomly selected
940 from each well.
941

942 **Stimulating cytoskeletal alignment, matrix deposition, and gap junction formation**
943 B6 and MRL/MpJ cells were seeded (2,000 cells/well) onto uncoated substrates and
944 cultured in full-serum media for 3 or 7 days. Media was changed every 2 days. To compare
945 baseline behavior for cytoskeletal alignment, matrix deposition, intercellular
946 communication, and myofibroblast activity, cells were stained for F-actin, fibronectin,
947 collagen I, Cx-43 gap junctions, and αSMA, respectively. Cytoskeletal alignment was
948 calculated as the local coherency/alignment index of F-actin stress fibers averaged over five
949 elliptical regions of interest (ROIs) for each representative image using the OrientationJ
950 (80) plugin. A coherency value of 1 indicates high anisotropy with perfectly aligned fibers,
951 whereas a value close to 0 indicates high isotropy with no preferential fiber alignment. Cx-
952 43 levels were measured as the integrated density normalized to cell number. Fibronectin
953 fibril alignment was similarly analyzed as described above. Fibronectin and collagen I
954 deposition were measured by normalizing the integrated density to the cell number of each
955 representative image. Myofibroblast activity was measured total αSMA integrated density.
956 Fibronectin and collagen I thickness were measured as the maximum intensity projection of
957 Z-stack images ($N = 3$ and $n = 27$ Z-stacks per group). All other outcome measures were
958 analyzed with $N = 3$ per group and up to $n = 45$ images per group with an equal number of
959 images randomly taken in each well.
960
961 To assess whether MRL/MpJ components are capable of shifting confluent B6 cells
962 toward an MRL/MpJ-like phenotype, B6 and MRL/MpJ cells were seeded (7,500
963 cells/well) onto uncoated or dPECM-coated substrates in full-serum media and allowed to
964 adhere for 24 hours. Cells were then cultured in either low-serum or secretome-media for
965 7 days. Media was changed every 2 days. Cytoskeletal alignment, matrix deposition,
966 intercellular communication, and myofibroblast activity were assessed by staining and
967 analyzing cells for F-actin, fibronectin, Cx-43, and αSMA. Cells were also stained for
968 collagen I deposition by measuring the integrated density normalized to cell number.
969 Fibronectin fibril alignment could not be analyzed due to insufficient ECM deposition
970 under low-serum culture conditions. All outcome measures were analyzed with $N = 3$ per
971 group and up to $n = 45$ images per group with an equal number of images randomly taken
972 in each well.
973
974 **Development of recombinant protein therapeutic and functional activity on rat cells**
975 Proteomic analyses of the mouse patellar tendon (MRL/MpJ 1-week dPECM compared to
976 B6 uninjured dECM) and secretome identified proteins of interest (POIs) for in vitro
977 investigation. Structural POIs with at least two unique peptides and that were $\geq$ 2-fold
978 higher in the MRL/MpJ 1-week dPECM ($P \leq 0.1$) were collectively applied onto collagen
979 I-coated substrates. Soluble POIs with at least two detected samples and that were $\geq$ 1.2-
980 fold higher ($P \leq 0.05$) were supplemented in low-serum media. A candidate panel of 29
981 POIs (10 structural and 19 soluble) were identified, 17 of which were evaluated as a
982 preliminary subset in this study (**Table 1**). All POIs were prepared fresh from the same
983 batch of stock solution to minimize the impact of freeze-thawing on protein stability.
984 Structural POIs were administered by first applying acid soluble proteins (in 0.1 M
985 AcOH) onto an existing base collagen I coating (50 µg/mL) overnight at 4°C. After
986 washing twice with 1X PBS to remove residual acid, non-acid soluble POIs were then
987 applied (in 1X PBS) overnight at 4°C. After washing twice again with 1X PBS, SD
988 tenocytes were seeded (750 cells/well) onto POI-coated substrates in full-serum media and
989 allowed to adhere for 18-24 hours.
990

To assess whether the recombinant protein therapeutic elicits a similar effect as MRL-derived components across different species of tenocytes, the following experimental groups were evaluated for single-cell morphology and confluent cell experiments: (1) rat cells alone, (2) cells cultured with dPECM (B6 uninjured or MRL/MpJ 1-week provisional) and secretome (B6 or MRL/MpJ), and (3) cells cultured with the POIs. For single-cell experiments, adhered SD tenocytes were serum starved in low-serum media for 24 hours and cultured in either low-serum or soluble POI-containing media for 24 hours. For confluent cell experiments, adhered SD tenocytes were cultured in either low-serum or soluble POI-containing media for 7 days. Media was changed every 2 days.

Rat single-cell morphology, cytoskeletal protrusion metrics, and aSMA integrated density were analyzed as described above ($N = 3$ and $n = 72$ cells per group). Cytoskeletal alignment and fibronectin deposition were analyzed as described above ($N = 3$ and $n = 45$ images per group).

Statistical Analysis

Baseline comparisons between B6 and MRL/MpJ cells or B6 and rat cells were performed using a Welch's *t*-test for single-cell morphology and confluent cell parameters, a Mann-Whitney *U* test for integrated density data, a Kolmogorov–Smirnov test for number of cytoskeletal protrusions, or a Student's *t*-test for all other outcome measures. Comparisons between treatment groups were performed using a one-way Welch ANOVA with Games-Howell's multiple comparisons test for single-cell morphology and confluent cell parameters, or a Kruskal-Wallis test with Dunn's multiple comparisons test for integrated density data. Cell senescence and population growth kinetics were compared between mouse genotypes and passage numbers using a two-way analysis of variance (ANOVA) with Bonferroni or Sidak multiple comparisons test. The Shapiro-Wilk test was performed to test for normality. All statistical analyses were performed using GraphPad Prism 9.3.1 (GraphPad Software, La Jolla, CA) unless specified otherwise. Statistical significance was set at $\alpha = 0.05$. Data are shown as mean $\pm$ standard error of the mean (SEM).

References

1. McCormick, Anna; Fleming, Douglas; Charlton, J. Pain in the hand and wrist Assessing health needs in primary care Morbidity study from general practice. *BMJ* **310,** 1995 (1995).
2. Galatz, L. M., Ball, C. M., Teefey, S. A., Middleton, W. D. & Yamaguchi, K. The Outcome and Repair Integrity of Completely Arthroscopically Repaired Large and Massive Rotator Cuff Tears. *Journal of Bone and Joint Surgery - Series A* **86,** 219–224 (2004).
3. Yang, G., Rothrauff, B. B. & Tuan, R. S. Tendon and ligament regeneration and repair: Clinical relevance and developmental paradigm. *Birth Defects Research Part C - Embryo Today: Reviews* **99,** 203–222 (2013).

1031 4. Andarawis-Puri, N., Flatow, E. L. & Soslowsky, L. J. Tendon basic science: Development,
1032 repair, regeneration, and healing. *Journal of Orthopaedic Research* **33,** 780–784 (2015).
1033 5. Le, A. D. K., Enweze, L., DeBaun, M. R. & Dragoo, J. L. Current Clinical Recommendations
1034 for Use of Platelet-Rich Plasma. *Current Reviews in Musculoskeletal Medicine* **11,** 624–634
1035 (2018).
1036 6. Kearney, R. S. *et al.* Effect of Platelet-Rich Plasma Injection vs Sham Injection on Tendon
1037 Dysfunction in Patients with Chronic Midportion Achilles Tendinopathy: A Randomized
1038 Clinical Trial. *JAMA - Journal of the American Medical Association* **326,** 137–144 (2021).
1039 7. Bedelbaeva, K. *et al.* Lack of p21 expression links cell cycle control and appendage
1040 regeneration in mice. *Proceedings of the National Academy of Sciences of the United States of*
1041 *America* **107,** 5845–5850 (2010).
1042 8. Rai, M. F. & Sandell, L. J. Regeneration of articular cartilage in healer and non-healer mice.
1043 *Matrix Biology* **39,** 50–55 (2014).
1044 9. Sereysky, J. B., Flatow, E. L. & Andarawis-Puri, N. Musculoskeletal regeneration and its
1045 implications for the treatment of tendinopathy. *International Journal of Experimental*
1046 *Pathology* **94,** 293–303 (2013).
1047 10. Lalley, A. L. *et al.* Improved biomechanical and biological outcomes in the MRL/MpJ murine
1048 strain following a full-length patellar tendon injury. *Journal of Orthopaedic Research* **33,**
1049 1693–1703 (2015).
1050 11. Paredes, J., Shiovitz, D. A., Andarawis-puri, N. & Sinai, M. Uncorrelated healing response of
1051 tendon and ear injuries in MRL highlight a role for the local tendon environment in driving
1052 scarless healing. *Connective Tissue Research* **59,** 472–482 (2018).
1053 12. Paredes, J., Marvin, J. C., Vaughn, B. & Andarawis-Puri, N. Innate tissue properties drive
1054 improved tendon healing in MRL/MpJ and harness cues that enhance behavior of canonical
1055 healing cells. *FASEB Journal* **34,** 8341–8356 (2020).

1056 13. George, N. S., Bell, R., Paredes, J. J., Taub, P. J. & Andarawis-Puri, N. Superior mechanical
1057 recovery in male and female MRL/MpJ tendons is associated with a unique genetic profile.
1058 *Journal of Orthopaedic Research* **39,** 1344–1354 (2021).
1059 14. Kallenbach, J. G. *et al.* Altered TGFB1 regulated pathways promote accelerated tendon
1060 healing in the superhealer MRL/MpJ mouse Short Title: Differential Transcriptional
1061 Regulation of Tendon Healing in MRL Mouse. *Scientific Reports* **12,** 2021.02.08.430308
1062 (2022).
1063 15. Chatterjee, M., Acosta, A., Taub, P. J. & Andarawis-Puri, N. Enhanced healing outcomes in
1064 MRL/MpJ mouse tissues conserved in insertion site following surgical repair. *Journal of*
1065 *Shoulder and Elbow Surgery* **31,** e593–e602 (2022).
1066 16. Paredes, J., Pekmezian, A. & Andarawis-Puri, N. MRL/MpJ tendon matrix-derived
1067 therapeutic promotes improved healing outcomes in scar-mediated canonical tendon healing.
1068 *Journal of Orthopaedic Research* 1–13 (2020). doi:10.1002/jor.24754
1069 17. Svitkina, T. The actin cytoskeleton and actin-based motility. *Cold Spring Harbor*
1070 *Perspectives in Biology* **10,** (2018).
1071 18. Geiger, B., Spatz, J. P. & Bershadsky, A. D. Environmental sensing through focal adhesions.
1072 *Nature Reviews Molecular Cell Biology* **10,** 21–33 (2009).
1073 19. Parsons, J. T., Horwitz, A. R. & Schwartz, M. A. Cell adhesion: Integrating cytoskeletal
1074 dynamics and cellular tension. *Nature Reviews Molecular Cell Biology* **11,** 633–643 (2010).
1075 20. Thievessen, I. *et al.* Vinculin-actin interaction couples actin retrograde flow to focal
1076 adhesions, but is dispensable for focal adhesion growth. *Journal of Cell Biology* **202,** 163–
1077 177 (2013).
1078 21. Jansen, K. A., Atherton, P. & Ballestrem, C. Mechanotransduction at the cell-matrix interface.
1079 *Seminars in Cell and Developmental Biology* **71,** 75–83 (2017).
1080 22. Dupont, S. *et al.* Role of YAP/TAZ in mechanotransduction. *Nature* **474,** 179–184 (2011).

1081 23. Wada, K. I., Itoga, K., Okano, T., Yonemura, S. & Sasaki, H. Hippo pathway regulation by
1082 cell morphology and stress fibers. *Development* **138,** 3907–3914 (2011).
1083 24. Driscoll, T. P., Cosgrove, B. D., Heo, S. J., Shurden, Z. E. & Mauck, R. L. Cytoskeletal to
1084 Nuclear Strain Transfer Regulates YAP Signaling in Mesenchymal Stem Cells. *Biophysical*
1085 *Journal* **108,** 2783–2793 (2015).
1086 25. Nardone, G. *et al.* YAP regulates cell mechanics by controlling focal adhesion assembly.
1087 *Nature Communications* **8,** (2017).
1088 26. Danen, E. H. J., Sonneveld, P., Brakebusch, C., Fässler, R. & Sonnenberg, A. The
1089 fibronectin-binding integrins α5β1 and αvβ3 differentially modulate RhoA-GTP loading,
1090 organization of cell matrix adhesions, and fibronectin fibrillogenesis. *Journal of Cell Biology*
1091 **159,** 1071–1086 (2002).
1092 27. Wierzbicka-Patynowski, I. & Schwarzbauer, J. E. The ins and outs of fibronectin matrix
1093 assembly. *Journal of Cell Science* **116,** 3269–3276 (2003).
1094 28. Ilić, D. *et al.* FAK promotes organization of fibronectin matrix and fibrillar adhesions.
1095 *Journal of Cell Science* **117,** 177–187 (2004).
1096 29. Filigheddu, N. *et al.* Fibronectin Matrix Assembly Requires Distinct Contributions from Rho
1097 Kinases I and -II. *Molecular biology of the cell* **18,** 986–994 (2007).
1098 30. Wang, E. Senescent Human Fibroblasts Resist Programmed Cell Death, and Failure to
1099 Suppress bell Is Involved. *Cancer Research* **55,** 2284–2292 (1995).
1100 31. Sasaki, M., Kumazaki, T., Takano, H., Nishiyama, M. & Mitsui, Y. Senescent cells are
1101 resistant to death despite low Bcl-2 level. *Mechanisms of Ageing and Development* **122,**
1102 1695–1706 (2001).
1103 32. Bedelbaeva, K. *et al.* Lack of p21 expression links cell cycle control and appendage
1104 regeneration in mice. *Proceedings of the National Academy of Sciences of the United States of*
1105 *America* **107,** 5845–5850 (2010).

1106 33. Jablonski, C. L., Besler, B. A., Ali, J. & Krawetz, R. J. p21−/− Mice Exhibit Spontaneous
1107 Articular Cartilage Regeneration Post-Injury. *Cartilage* **13,** 1608S-1617S (2021).
1108 34. Byron, A., Humphries, J. D. & Humphries, M. J. Defining the extracellular matrix using
1109 proteomics. *International Journal of Experimental Pathology* **94,** 75–92 (2013).
1110 35. Gwam, C., Mohammed, N. & Ma, X. Stem cell secretome, regeneration, and clinical
1111 translation: a narrative review. *Annals of Translational Medicine* **9,** 70–70 (2021).
1112 36. Warden, S. J. Animal models for the study of tendinopathy. *British Journal of Sports*
1113 *Medicine* **41,** 232–240 (2007).
1114 37. Hast, M. W., Zuskov, A. & Soslowsky, L. J. The role of animal models in tendon research.
1115 *Bone and Joint Research* **3,** 193–202 (2014).
1116 38. Badylak, S. F., Freytes, D. O. & Gilbert, T. W. Extracellular matrix as a biological scaffold
1117 material: Structure and function. *Acta Biomaterialia* **5,** 1–13 (2009).
1118 39. Hussey, G. S., Dziki, J. L. & Badylak, S. F. Extracellular matrix-based materials for
1119 regenerative medicine. *Nature Reviews Materials* 1 (2018). doi:10.1038/s41578-018-0023-x
1120 40. L., P. K. *et al.* The mesenchymal stem cell secretome: A new paradigm towards cell-free
1121 therapeutic mode in regenerative medicine. *Cytokine and Growth Factor Reviews* **46,** 1–9
1122 (2019).
1123 41. Zhang, Y. *et al.* Drug-induced regeneration in adult mice. **7,** (2015).
1124 42. Grinstein, M. *et al.* A quiescent resident progenitor pool is the central organizer of tendon
1125 healing. *bioRxiv* 1–62 (2022). doi:10.1101/2022.02.02.478533
1126 43. Poulsen, R. C. *et al.* Glucocorticoids induce senescence in primary human tenocytes by
1127 inhibition of sirtuin 1 and activation of the p53/p21 pathway: In vivo and in vitro evidence.
1128 *Annals of the Rheumatic Diseases* **73,** 1405–1413 (2014).
1129 44. Chen, M. *et al.* AQP1 modulates tendon stem/progenitor cells senescence during tendon
1130 aging. *Cell Death and Disease* **11,** (2020).

1131 45. Wang, C. *et al.* Inhibition of IKKβ/NF-κB signaling facilitates tendinopathy healing by
1132 rejuvenating inflamm-aging induced tendon-derived stem/progenitor cell senescence.
1133 *Molecular Therapy - Nucleic Acids* **27,** 562–576 (2022).
1134 46. Stowe, E. J., Keller, M. R. & Connizzo, B. K. Cellular Senescence Impairs Tendon
1135 Extracellular Matrix Remodeling in Response to Mechanical Unloading. Preprint at
1136 https://doi.org/10.1101/2023.12.22.572594 (2023)
1137 47. Basisty, N. *et al.* A Proteomic Atlas of Senescence-Associated Secretomes for Aging
1138 Biomarker Development. *SSRN Electronic Journal* 1–26 (2019). doi:10.2139/ssrn.3380253
1139 48. Da Silva-Álvarez, S. *et al.* Cell senescence contributes to tissue regeneration in zebrafish.
1140 *Aging Cell* **19,** 1–5 (2020).
1141 49. Antelo-Iglesias, L., Picallos-Rabina, P., Estévez-Souto, V., Da Silva-Álvarez, S. & Collado,
1142 M. The role of cellular senescence in tissue repair and regeneration. *Mechanisms of Ageing*
1143 *and Development* **198,** (2021).
1144 50. Jeon, O. H. *et al.* Local clearance of senescent cells attenuates the development of post-
1145 traumatic osteoarthritis and creates a pro-regenerative environment. *Nature Medicine* **23,**
1146 775–781 (2017).
1147 51. Wan, M., Gray-Gaillard, E. F. & Elisseeff, J. H. Cellular senescence in musculoskeletal
1148 homeostasis, diseases, and regeneration. *Bone Research* **9,** 1–12 (2021).
1149 52. Alisafaei, A. F., Shakiba, D., Iannucci, L. E. & Matthew, D. Tension anisotropy drives
1150 phenotypic transitions of cells via two-way cell-ECM feedback. *bioRxiv* 1–15 (2022).
1151 doi:10.1101/2022.03.13.484154
1152 53. Izu, Y. *et al.* Collagen XII mediated cellular and extracellular mechanisms regulate
1153 establishment of tendon structure and function. *Matrix Biology* **95,** 52–67 (2021).
1154 54. Banes, A. J. *et al.* Gap junctions regulate responses of tendon cells ex vivo to mechanical
1155 loading. *Clinical Orthopaedics and Related Research* **367,** 356–370 (1999).

1156 55. Waggett, A. D., Benjamin, M. & Ralphs, J. R. Connexin 32 and 43 gap junctions
1157 differentially modulate tenocyte response to cyclic mechanical load. *European Journal of*
1158 *Cell Biology* **85,** 1145–1154 (2006).
1159 56. Theodossiou, S. K., Murray, J. B. & Schiele, N. R. Cell-cell junctions in developing and adult
1160 tendons. *Tissue Barriers* **8,** (2020).
1161 57. Kubow, K. E. *et al.* Mechanical forces regulate the interactions of fibronectin and collagen i
1162 in extracellular matrix. *Nature Communications* **6,** (2015).
1163 58. Barker, T. H., Engler, A. J. & Jolla, L. The provisional matrix: setting the stage for tissue
1164 repair outcomes. *Matrix Biology* 1–4 (2018). doi:10.1016/j.matbio.2017.04.003.The
1165 59. Howell, K. *et al.* Novel Model of Tendon Regeneration Reveals Distinct Cell Mechanisms
1166 Underlying Regenerative and Fibrotic Tendon Healing. *Scientific Reports* **7,** 1–14 (2017).
1167 60. Best, K. T. & Loiselle, A. E. Scleraxis lineage cells contribute to organized bridging tissue
1168 during tendon healing and identify a subpopulation of resident tendon cells. *FASEB Journal*
1169 **33,** 8578–8587 (2019).
1170 61. Best, K. T. *et al.* NF-κB activation persists into the remodeling phase of tendon healing and
1171 promotes myofibroblast survival. *Science Signaling* **13,** (2020).
1172 62. Bi, Y. *et al.* Identification of tendon stem/progenitor cells and the role of the extracellular
1173 matrix in their niche. *Nature Medicine* **13,** 1219–1227 (2007).
1174 63. Valekova, I., Skalnikova, H. K., Jarkovska, K., Motlik, J. & Kovarova, H. in *Stem Cell*
1175 *Renewal and Cell-Cell Communication. Methods in Molecular Biology* (ed. Turksen, K.)
1176 **1212,** 39–63 (2014).
1177 64. Marvin, J. C., Brakewood, M. E., Poon, M. L. S. & Andarawis-Puri, N. Regenerative
1178 MRL/MpJ tendon cells exhibit sex differences in morphology, proliferation,
1179 mechanosensitivity, and cell–ECM organization. *Journal Orthopaedic Research* **41,** 2273–
1180 2286 (2023).

1181 65. Cho, Y. *et al.* CTRP3 exacerbates tendinopathy by dysregulating tendon stem cell
1182 differentiation and altering extracellular matrix composition. *Science Advances* **7,** (2021).
1183 66. Rovai, L. E., Herschman, H. R. & Smith, J. B. The murine neutrophil-chemoattractant
1184 chemokines LIX, KC, and MIP-2 have distinct induction kinetics, tissue distributions, and
1185 tissue-specific sensitivities to glucocorticoid regulation in endotoxemia. *Journal of Leukocyte*
1186 *Biology* **64,** 494–502 (1998).
1187 67. Ohtsuka, Y., Lee, J., Stamm, D. S. & Sanderson, I. R. MIP-2 secreted by epithelial cells
1188 increases neutrophil and lymphocyte recruitment in the mouse intestine. *Gut* **49,** 526–533
1189 (2001).
1190 68. Zins, S. R., Amare, M. F., Anam, K., Elster, E. A. & Davis, T. A. Wound trauma mediated
1191 inflammatory signaling attenuates a tissue regenerative response in MRL/MpJ mice. *Journal*
1192 *of Inflammation* **7,** 1–9 (2010).
1193 69. Song, J., Wu, C., Zhang, X. & Sorokin, L. M. In Vivo Processing of CXCL5 (LIX) by Matrix
1194 Metalloproteinase (MMP)-2 and MMP-9 Promotes Early Neutrophil Recruitment in IL-1β–
1195 Induced Peritonitis. *The Journal of Immunology* **190,** 401–410 (2013).
1196 70. Plant, T. *et al.* Semaphorin 3F signaling actively retains neutrophils at sites of inflammation.
1197 *Journal of Clinical Investigation* **130,** 3221–3237 (2020).
1198 71. Tarafder, S. *et al.* Tendon stem/progenitor cells regulate inflammation in tendon healing via
1199 JNK and STAT3 signaling. *FASEB Journal* **31,** 3991–3998 (2017).
1200 72. Seternes, O. M., Kidger, A. M. & Keyse, S. M. Dual-specificity MAP kinase phosphatases in
1201 health and disease. *Biochimica et Biophysica Acta - Molecular Cell Research* **1866,** 124–143
1202 (2019).
1203 73. Blache, U. *et al.* Inhibition of ERK 1/2 kinases prevents tendon matrix breakdown. *Scientific*
1204 *Reports* **11,** (2021).

1205 74. Marvin, J. C., Mochida, A., Paredes, J., Vaughn, B. & Andarawis-Puri, N. Detergent-Free
1206 Decellularization Preserves the Mechanical and Biological Integrity of Murine Tendon.
1207 *Tissue Engineering Part C: Methods* **28,** 646–655 (2022).
1208 75. Wipff, P. J. *et al.* The covalent attachment of adhesion molecules to silicone membranes for
1209 cell stretching applications. *Biomaterials* **30,** 1781–1789 (2009).
1210 76. Kuddannaya, S. *et al.* Surface chemical modification of poly(dimethylsiloxane) for the
1211 enhanced adhesion and proliferation of mesenchymal stem cells. *ACS Applied Materials and*
1212 *Interfaces* **5,** 9777–9784 (2013).
1213 77. Gannier, F., White, E., Lacampagne, A., Garnier, D. & Guennec, J.-Y. Le. Streptomycin
1214 reverses a large stretch induced increase in [Ca"'], in isolated guinea pig ventricular
1215 myocytes. *Cardiovascular Research* **28,** 1193–1198 (1994).
1216 78. Metsalu, T. & Vilo, J. ClustVis: A web tool for visualizing clustering of multivariate data
1217 using Principal Component Analysis and heatmap. *Nucleic Acids Research* **43,** W566–W570
1218 (2015).
1219 79. Horzum, U., Ozdil, B. & Pesen-Okvur, D. Step-by-step quantitative analysis of focal
1220 adhesions. *MethodsX* **1,** 56–59 (2014).
1221 80. Fonck, E. *et al.* Effect of aging on elastin functionality in human cerebral arteries. *Stroke* **40,**
1222 2552–2556 (2009).

1223 **Acknowledgments**

1224 We acknowledge K. Adebowale for assistance and insightful feedback in interpreting the
1225 single-cell actin cytoskeleton and focal adhesion data. We acknowledge C. Mendias and
1226 A. Shimpi for helpful discussions in interpreting the proteomics data. We also
1227 acknowledge Y. Wang for access to their lyophilizer. We acknowledge R. Bell and M.
1228 Pacheco for their contributions in developing the recombinant protein panel. We
1229 acknowledge E. Maloney for performing rat tenocyte isolations. We also acknowledge the
1230 Cornell Center for Animal Resources and Education (CARE) staff for animal care. All
1231 graphical schematics and illustrations were generated using BioRender.
1232
1233 **Funding:** This project was funded by: National Institutes of Health (NIH) and National
1234 Science Foundation (NSF).
1235
1236 NIH Grant R01AR068301 (NAP)

NIH Grant R21AR074602 (NAP)
NIH Grant R56AR077239 (NAP)
NIH Grant 1S10RR025502 (Cornell University Biotechnology Resource Center)
NSF GRFP DGE-1650441 (JCM)

Author contributions: https://www.elsevier.com/authors/policies-and-guidelines/credit-author-statement

Conceptualization: JCM, NAP
Methodology: JCM, NAP
Investigation: JCM, EJL, HC, DAS
Visualization: JCM, EJL, HC, DAS
Supervision: NAP
Writing—original draft: JCM
Writing—review & editing: JCM, NAP

JCM and NAP conceived the study and developed the hypotheses. JCM designed experiments and performed all protocol development, animal surgeries, and research. JCM and EJL carried out proteomics analyses and confocal microscopy experiments. JCM, EJL, and HC analyzed immunofluorescence and staining data. DAS performed and analyzed histological data. NAP supervised the work. JCM wrote the paper. JCM and NAP edited and revised the manuscript.

Competing interests: The authors declare that they have no competing interests.

Data and materials availability: All data are available in the main text or the supplementary materials. Raw data for all Quantibody experiments will be made publicly available for access upon publication.

Figures and Tables

1267 **Fig. 1. MRL/MpJ tenocytes demonstrate enhanced mechanosensitivity and cell**
1268 **migration and form more actin-rich, axon-like cellular protrusions compared**
1269 **to B6 tenocytes**. (**A**) Experimental design to assess characterize morphology and
1270 focal adhesion formation. (**B to E**) IF staining of F-actin (gray) and vinculin
1271 (green) of B6 and MRL/MpJ tenocytes cultured on collagen I-coated substrates
1272 (scale bar, 100 μm; 2X-magnified insets in the top-right corner of representative
1273 vinculin images). MRL/MpJ tenocytes formed more extensive cellular protrusions
1274 (C) that were accompanied by greater cell spreading and perimeter (D) and
1275 assembly of nascent focal adhesions compared to B6 tenocytes (E). (**F to H**)
1276 Experimental design to quantify tenocyte migration via wound scratch assays.
1277 Wound scratch analysis (F) showed that a significantly greater number of
1278 MRL/MpJ tenocytes than B6 tenocytes migrated on fibronectin-coated substrates
1279 after 12 hours post-scratch (G) despite comparable cell protrusion characteristics
1280 between cells cultured on collagen I and fibronectin (H). (**I**) Experimental design
1281 to assess YAP-mediated mechanosignaling. IF staining of phalloidin (grey) and
1282 YAP (magnified 3X in gray; green in merged representative images) of B6 and
1283 MRL/MpJ tenocytes cultured on collagen I-coated substrates (scale bar, 100 μm)
1284 with pharmacological inhibitors for actin polymerization (Lat-A), myosin II
1285 (blebbistatin), and ROCK (Y-27632). DMSO-treated cells served as a control. (**J**)
1286 At baseline, MRL/MpJ tenocytes displayed significantly higher YAP nuclear
1287 localization than B6 tenocytes. (**K**) Relative nuclear translocation of YAP
1288 (normalized to respective DMSO control mean) was significantly reduced in
1289 MRL/MpJ tenocytes compared to B6 tenocytes with inhibition of myosin II and
1290 ROCK. *$P < 0.05$, **$P < 0.01$, ***$P < 0.001$, ****$P < 0.0001$. Significance was
1291 determined using a Welch's t-test when comparing B6 and MRL/MpJ tenocytes, or
1292 a two-way ANOVA with post-hoc Bonferroni when comparing genotypes for each
1293 inhibitor for YAP data. Representative images shown for all staining experiments.

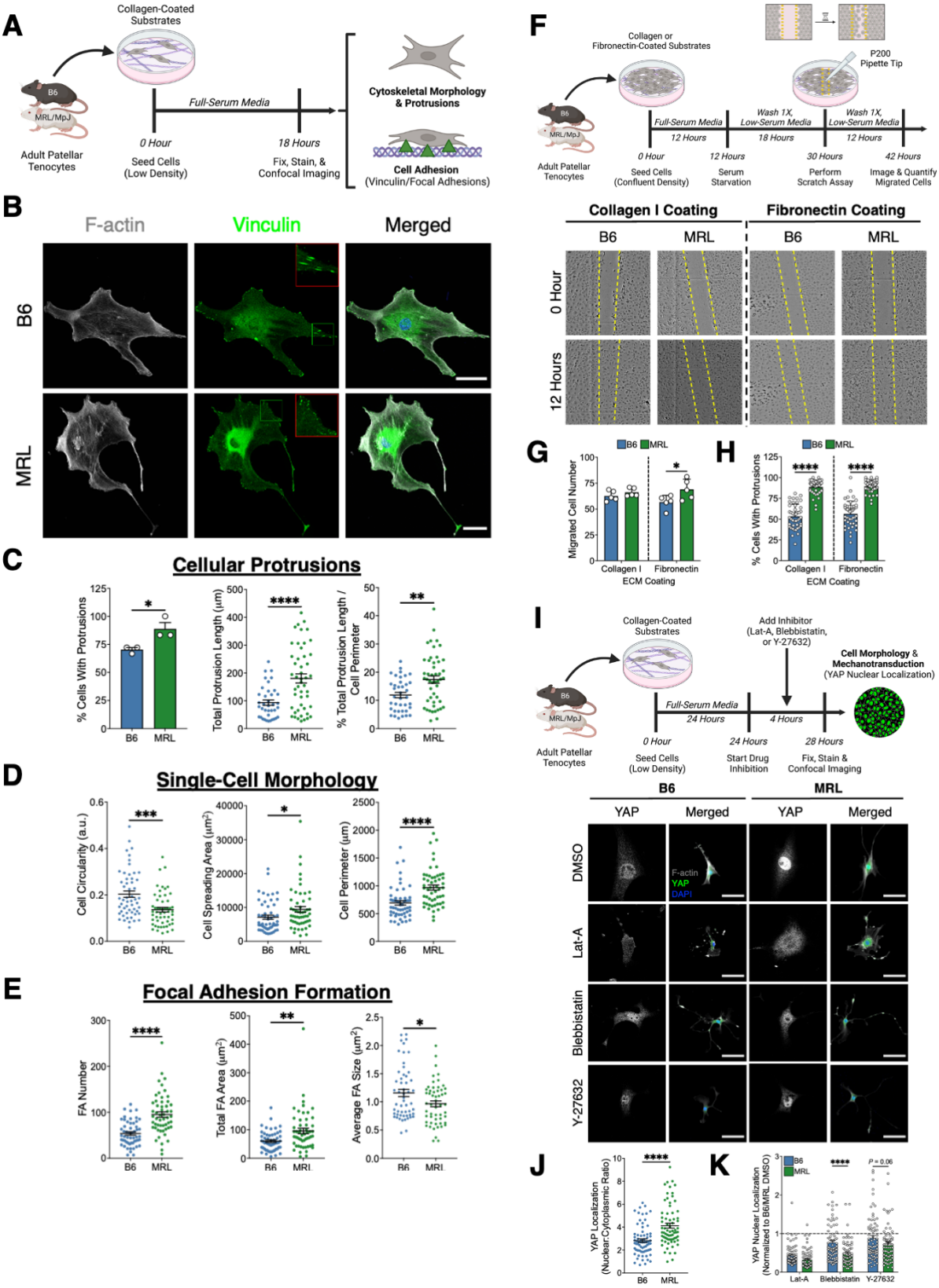
A
Collagen-Coated Substrates
B6
MRL/MpJ
Adult Patellar Tenocytes
Full-Serum Media
0 Hour
Seed Cells (Low Density)
18 Hours
Fix, Stain, & Confocal Imaging
Cytoskeletal Morphology & Protrusions
Cell Adhesion (Vinculin/Focal Adhesions)
B
F-actin
Vinculin
Merged
B6
MRL
C
Cellular Protrusions
% Cells With Protrusions
Total Protrusion Length (µm)
% Total Protrusion Length / Cell Perimeter
D
Single-Cell Morphology
Cell Circularity (a.u.)
Cell Spreading Area (µm²)
Cell Perimeter (µm)
E
Focal Adhesion Formation
FA Number
Total FA Area (µm²)
Average FA Size (µm²)
F
Collagen or Fibronectin-Coated Substrates
P200 Pipette Tip
Full-Serum Media
12 Hours
Wash 1X, Low-Serum Media
18 Hours
Wash 1X, Low-Serum Media
12 Hours
0 Hour
Seed Cells (Confluent Density)
12 Hours
Serum Starvation
30 Hours
Perform Scratch Assay
42 Hours
Image & Quantify Migrated Cells
Collagen I Coating
Fibronectin Coating
0 Hour
12 Hours
G
Migrated Cell Number
Collagen I
Fibronectin
ECM Coating
H
% Cells With Protrusions
I
Add Inhibitor (Lat-A, Blebbistatin, or Y-27632)
Cell Morphology & Mechanotransduction (YAP Nuclear Localization)
Full-Serum Media
24 Hours
4 Hours
24 Hours
Start Drug Inhibition
28 Hours
Fix, Stain & Confocal Imaging
YAP
Merged
DMSO
Lat-A
Blebbistatin
Y-27632
F-actin
DAPI
J
YAP Localization (Nuclear:Cytoplasmic Ratio)
K
YAP Nuclear Localization (Normalized to B6/MRL DMSO)
P = 0.06

1296 **Fig. 2. MRL/MpJ tenocytes promote cytoskeletal and cellular alignment, ECM**
1297 **deposition, and intercellular communication consisted with effective tendon**
1298 **healing outcomes *in vivo*.** (**A**) Experimental design to assess confluent tenocyte
1299 behavior after 7 days of culture in full-serum media. (**B to D**) IF staining of (B)
1300 connexin-43 (Cx-43, green) and F-actin (grey) in addition to (C) fibronectin
1301 (green), collagen I (cyan), and αSMA (gray) in confluent B6 and MRL/MpJ
1302 tenocytes (scale bar, 100 μm). MRL/MpJ tenocytes displayed greater cytoskeletal
1303 and matrix anisotropy, ECM fibrillogenesis, and arrangement of nuclei in linear
1304 arrays (indicated by the dashed yellow line) compared to B6 tenocytes. (**D to F**)
1305 MRL/MpJ tenocytes exhibited significantly greater F-actin and fibronectin
1306 coherency/alignment (D), fibronectin and collagen I deposition (E), and cell
1307 number and Cx-43 levels (F) than B6 tenocytes. (**G**) IF staining of Cx-43 (green)
1308 and F-actin (grey) at moderate cell densities after 3 days of culture revealed that
1309 gap junctions localize along the length and tips of actin-rich cellular protrusions
1310 (indicated by yellow arrowheads) to facilitate intercellular communication. (**H**)
1311 αSMA expression remained comparable between B6 and MRL/MpJ tenocytes
1312 after 3 and 7 days of culture suggesting that increased myofibroblast activation
1313 does not drive improved structural organization *in vitro*. $^{*}P < 0.05$, $^{**}P < 0.01$,
1314 $^{***}P < 0.001$, $^{****}P < 0.0001$. Significance was determined using a Welch's t-test
1315 when comparing coherency, ECM thickness, or cell number data. Integrated
1316 density data on a per cell basis further normalized to the B6 mean was compared
1317 using a non-parametric Mann-Whitney *U* test. Representative images shown for all
1318 staining experiments.
1319
1320
1321

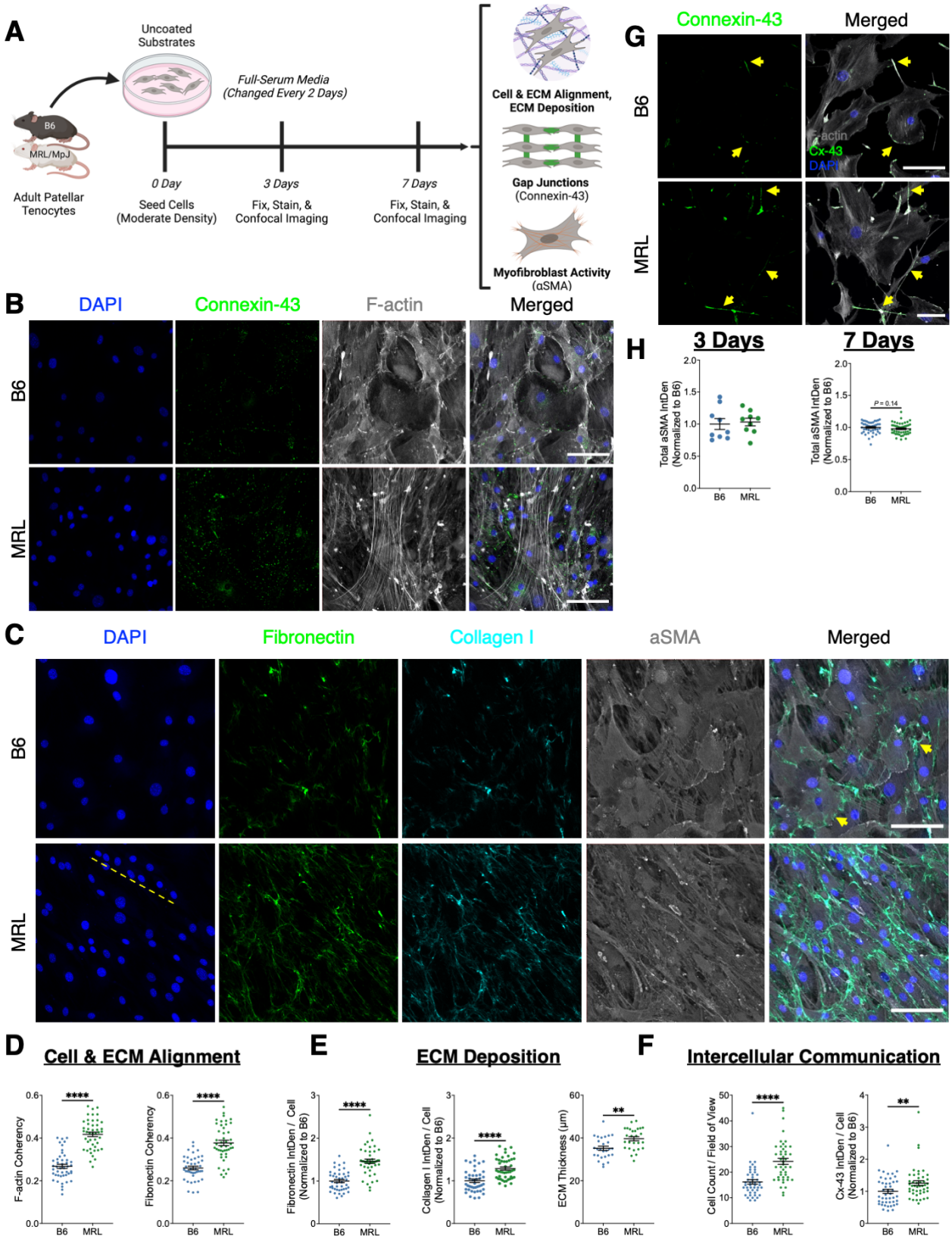
A
Uncoated Substrates
Full-Serum Media (Changed Every 2 Days)
B6
MRL/MpJ
Adult Patellar Tenocytes
0 Day
Seed Cells (Moderate Density)
3 Days
Fix, Stain, & Confocal Imaging
7 Days
Fix, Stain, & Confocal Imaging
Cell & ECM Alignment, ECM Deposition
Gap Junctions (Connexin-43)
Myofibroblast Activity (αSMA)
B
DAPI
Connexin-43
F-actin
Merged
B6
MRL
C
DAPI
Fibronectin
Collagen I
aSMA
Merged
B6
MRL
D
Cell & ECM Alignment
F-actin Coherency
Fibonectin Coherency
E
ECM Deposition
Fibronectin IntDen / Cell (Normalized to B6)
Collagen I IntDen / Cell (Normalized to B6)
ECM Thickness (μm)
F
Intercellular Communication
Cell Count / Field of View
Cx-43 IntDen / Cell (Normalized to B6)
B6
MRL
G
Connexin-43
Merged
B6
MRL
F-actin
Cx-43
DAPI
H
3 Days
7 Days
Total aSMA IntDen (Normalized to B6)
P = 0.14
B6
MRL

1322

1323 **Fig. 3. Quantitative proteomics reveal biological signatures enriched in the**
1324 **MRL/MpJ tenocyte secretome that are conserved across static and dynamic**
1325 **culture compared to those of B6.** (**A**) Schematic illustration of primary mouse
1326 tenocyte secretome collection under static and dynamic culture conditions for
1327 RayBiotech quantitative proteomics analyses. (**B**) Breakdown of differentially
1328 expressed proteins (DEPs) upregulated in the B6 (in blue) and MRL/MpJ (in red)
1329 tenocyte secretomes. (**C**) Principal components analysis (PCA) showed distinct
1330 clustering of static secretome samples by genotype (left) but overlap of dynamic
1331 secretome samples (right). (**D and E**) Heat maps of Z-score hierarchical clustering
1332 based on Euclidean distance for rows and volcano plots of the static (D) and
1333 dynamic (E) secretomes. Blue and green bars underneath heat maps denote B6 and
1334 MRL/MpJ biological replicates, respectively. (**F to H**) Comparative ingenuity
1335 pathway analysis (IPA) of the static and dynamic secretomes predicted similar
1336 activation Z-score patterns for the top 10 diseases and functions (F) and canonical
1337 pathways (G) but contrasting activation states for 8 of 10 upstream regulators (H).
1338 (**I**) Heat map visualizing relative changes in protein concentration within each
1339 genotype for cytokine targets shared between the static and dynamic secretomes.
1340 Blue and red colors indicate annotations predicted to be activated or enriched in B6
1341 or MRL/MpJ secretomes, respectively. Black boxes indicate annotations or
1342 cytokines that were not detected.
1343

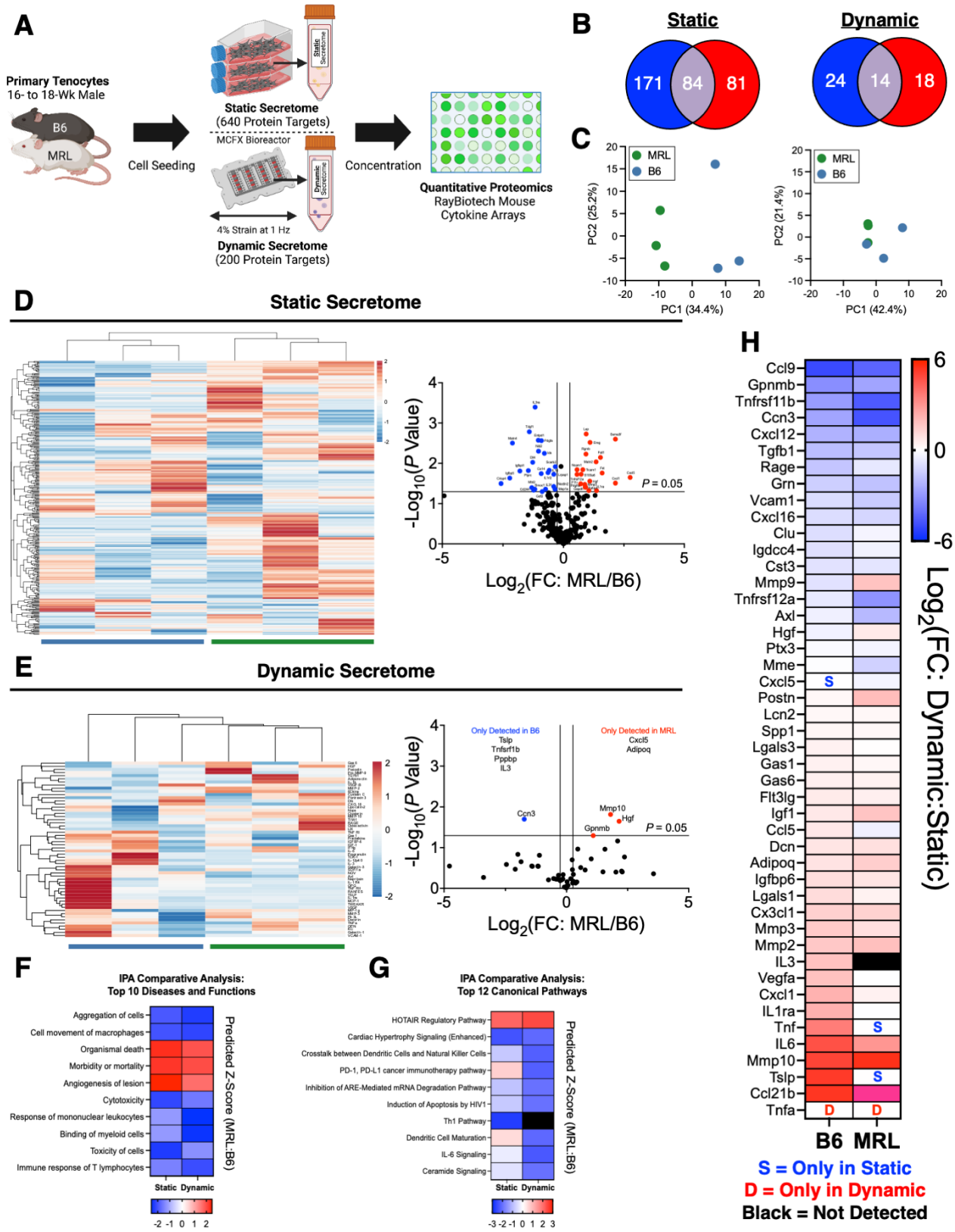
A
Primary Tenocytes
16- to 18-Wk Male
B6
MRL
Cell Seeding
Static Secretome
(640 Protein Targets)
MCFX Bioreactor
4% Strain at 1 Hz
Dynamic Secretome
(200 Protein Targets)
Concentration
Quantitative Proteomics
RayBiotech Mouse
Cytokine Arrays
B
Static
Dynamic
171
84
81
24
14
18
C
MRL
B6
PC2 (25.2%)
PC1 (34.4%)
PC2 (21.4%)
PC1 (42.4%)
D
Static Secretome
-Log10(P Value)
Log2(FC: MRL/B6)
P = 0.05
E
Dynamic Secretome
Only Detected in B6
Tslp
Tnfsrf1b
Pppbp
IL3
Only Detected in MRL
Cxcl5
Adipoq
Ccn3
Mmp10
Hgf
Gpnmb
F
IPA Comparative Analysis:
Top 10 Diseases and Functions
Aggregation of cells
Cell movement of macrophages
Organismal death
Morbidity or mortality
Angiogenesis of lesion
Cytotoxicity
Response of mononuclear leukocytes
Binding of myeloid cells
Toxicity of cells
Immune response of T lymphocytes
Static
Dynamic
Predicted Z-Score (MRL:B6)
G
IPA Comparative Analysis:
Top 12 Canonical Pathways
HOTAIR Regulatory Pathway
Cardiac Hypertrophy Signaling (Enhanced)
Crosstalk between Dendritic Cells and Natural Killer Cells
PD-1, PD-L1 cancer immunotherapy pathway
Inhibition of ARE-Mediated mRNA Degradation Pathway
Induction of Apoptosis by HIV1
Th1 Pathway
Dendritic Cell Maturation
IL-6 Signaling
Ceramide Signaling
H
Ccl9
Gpnmb
Tnfrsf11b
Ccn3
Cxcl12
Tgfb1
Rage
Grn
Vcam1
Cxcl16
Clu
Igdcc4
Cst3
Mmp9
Tnfrsf12a
Axl
Hgf
Ptx3
Mme
Cxcl5
Postn
Lcn2
Spp1
Lgals3
Gas1
Gas6
Flt3lg
Igf1
Ccl5
Dcn
Adipoq
Igfbp6
Lgals1
Cx3cl1
Mmp3
Mmp2
IL3
Vegfa
Cxcl1
IL1ra
Tnf
IL6
Mmp10
Tslp
Ccl21b
Tnfa
B6
MRL
Log2(FC: Dynamic:Static)
S = Only in Static
D = Only in Dynamic
Black = Not Detected

1350
1351 **Fig. 4. An adult population MRL/MpJ tenocytes undergo increased proliferative and**
1352 **apoptotic activity compared to B6 tenocytes**. (**A**) Experimental design to characterize
1353 cellular senescence and the growth kinetics of B6 and MRL/MpJ tenocytes. (**B and C**) B6
1354 tenocytes progressively accumulated ß-galactosidase (ß-gal) activity associated with
1355 cellular senescence in response to replicative stress induced by serial passages (P3-P5; B),
1356 whereas MRL/MpJ tenocytes maintained a non-senescent phenotype (C). (**D)** Population
1357 growth kinetics are diminished in B6 as compared to MRL/MpJ tenocytes at P5 as
1358 evidenced by significantly increased population doubling time (PDT) and decreased
1359 cumulative population doubling (CPD). (**E to G**) Immunohistochemical (IHC) staining of
1360 Ki-67 and cleaved caspase-3 found significantly increased cell proliferation (F) and
1361 apoptosis (G), respectively, in MRL/MpJ tendons compared to B6 tendons at 1 and 4
1362 weeks (F) after acute injury *in vivo* (scale bar, 50 µm; arrowheads indicate positively-
1363 stained cells; all sections were counterstained with toluidine blue). (**H**) Experimental
1364 design to measure DNA damage and p21 expression in B6 and MRL/MpJ tenocytes.
1365 Immunofluorescence (IF) staining revealed similar intrinsic expression of p21(green) and
1366 DNA damage (indicated by γH2AX-positive foci, magenta) between B6 and MRL/MpJ
1367 tenocytes (scale bar, 100 µm). $^{*}P < 0.05$, $^{**}P < 0.01$, $^{****}P < 0.0001$. Significance was
1368 determined using a two-way analysis of variance (ANOVA) with post-hoc Bonferroni or
1369 Šidák for *in vitro* assays, or an unpaired Student's t-test when comparing genotypes at
1370 each timepoint for IHC data. Representative images shown for all staining experiments.
1371

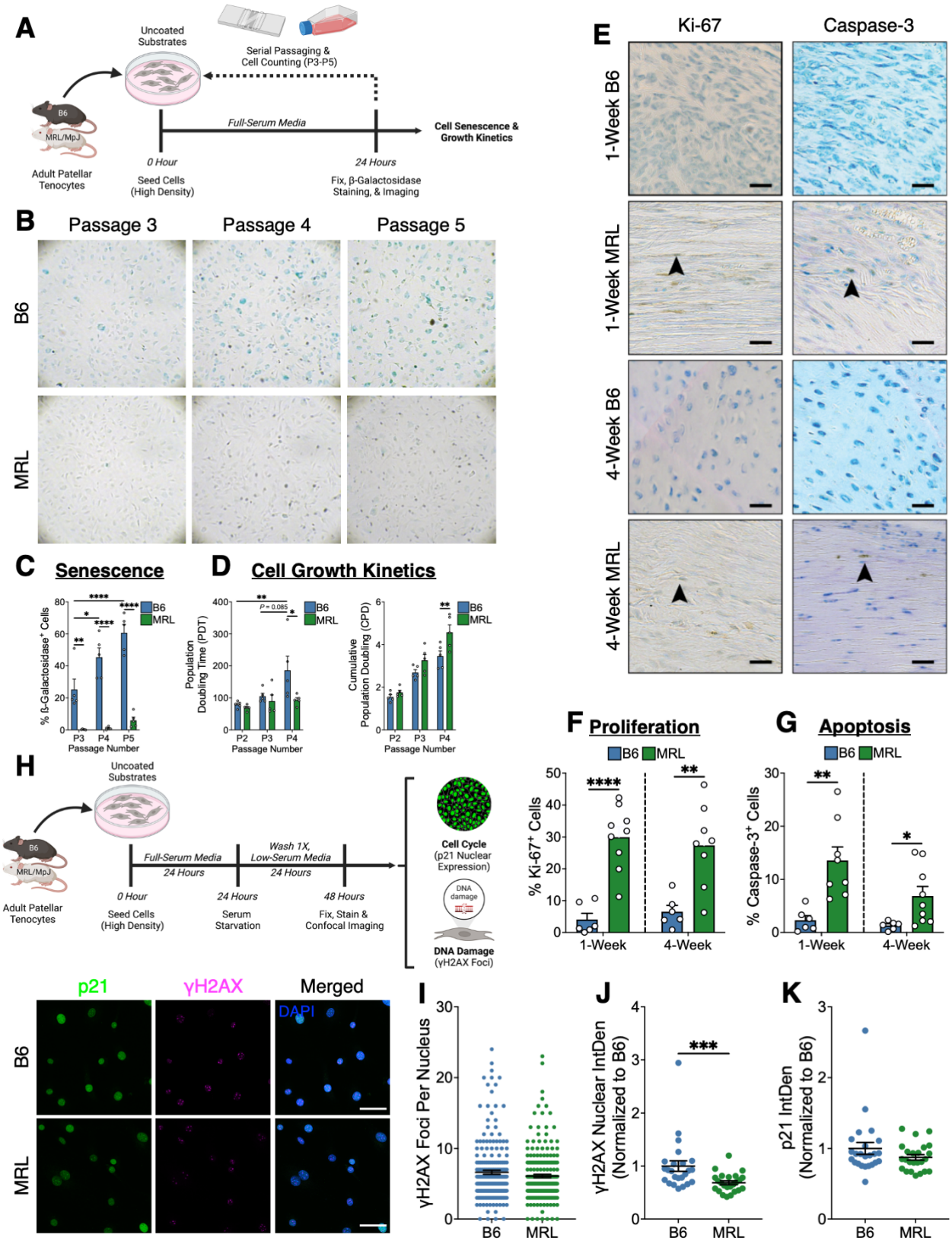
A
Uncoated Substrates
Serial Passaging & Cell Counting (P3-P5)
B6
MRL/MpJ
Adult Patellar Tenocytes
Full-Serum Media
Cell Senescence & Growth Kinetics
0 Hour
Seed Cells (High Density)
24 Hours
Fix, β-Galactosidase Staining, & Imaging
B
Passage 3
Passage 4
Passage 5
B6
MRL
C
Senescence
% β-Galactosidase+ Cells
B6
MRL
P3
P4
P5
Passage Number
D
Cell Growth Kinetics
Population Doubling Time (PDT)
P = 0.085
Cumulative Population Doubling (CPD)
P2
P3
P4
E
Ki-67
Caspase-3
1-Week B6
1-Week MRL
4-Week B6
4-Week MRL
F
Proliferation
% Ki-67+ Cells
1-Week
4-Week
G
Apoptosis
% Caspase-3+ Cells
H
Uncoated Substrates
Full-Serum Media
24 Hours
Wash 1X, Low-Serum Media
24 Hours
0 Hour
Seed Cells (High Density)
24 Hours
Serum Starvation
48 Hours
Fix, Stain & Confocal Imaging
Cell Cycle (p21 Nuclear Expression)
DNA damage
DNA Damage (γH2AX Foci)
p21
γH2AX
Merged
DAPI
I
γH2AX Foci Per Nucleus
J
γH2AX Nuclear IntDen (Normalized to B6)
K
p21 IntDen (Normalized to B6)

1374 **Fig. 5. B6 and MRL/MpJ tenocytes treated with a combination of MRL/MpJ-derived**
1375 **decellularized provisional ECM and secretome achieve comparable**
1376 **morphologies and cellular mechanotransduction**. (**A**) Experimental design and
1377 *in vitro* culture model of single-cell experiments for tenocytes cultured on dPECM
1378 with tenocyte-sourced secretome (henceforth referred to as 'components'). (**B**)
1379 Representative cell outlines of B6 and MRL/MpJ tenocytes cultured with B6 or
1380 MRL/MpJ-derived components (scale bar, 100 μm) to visualize cytoskeletal
1381 morphology and cellular protrusions. (**C**) IF staining of F-actin (grey) and vinculin
1382 (green) of treated B6 and MRL/MpJ tenocytes. (**D to F**) Cellular protrusion
1383 characteristics (D), single-cell morphological parameters (E), and focal adhesion
1384 profiles (F) are identical between B6 and MRL/MpJ tenocytes treated with
1385 MRL/MpJ-derived components and significantly different from B6 tenocytes
1386 treated with B6-derived components. (**g**) Representative cell outlines of B6
1387 tenocytes cultured with MRL/MpJ-derived components (scale bar, 200 μm). Cells
1388 with greater protrusion numbers and total protrusion lengths were associated with
1389 increased myofibroblast activity as visualized by dark blue colors indicating higher
1390 αSMA expression (relative to B6 mean). (**H and I**) MRL/MpJ-derived components
1391 promoted significantly greater αSMA expression (H) in B6 tenocytes but not cell
1392 proliferation (I) compared to B6-derived components or B6 cells cultured on
1393 collagen I-coated substrates. *$P < 0.05$, **$P < 0.01$, ***$P < 0.001$, ****$P <$
1394 0.0001. Significance was determined using a one-way Welch's ANOVA with post-
1395 hoc Games-Howell for cell morphology and focal adhesion data. For cellular
1396 protrusion data, significance was determined using a one-way ANOVA with post-
1397 hoc Tukey (percentage of cells with protrusions) or Kruskal-Wallis test with post-
1398 hoc Dunn's (number of protrusions and normalized total protrusion length).
1399 Representative images shown for all staining experiments.
1400
1401
1402

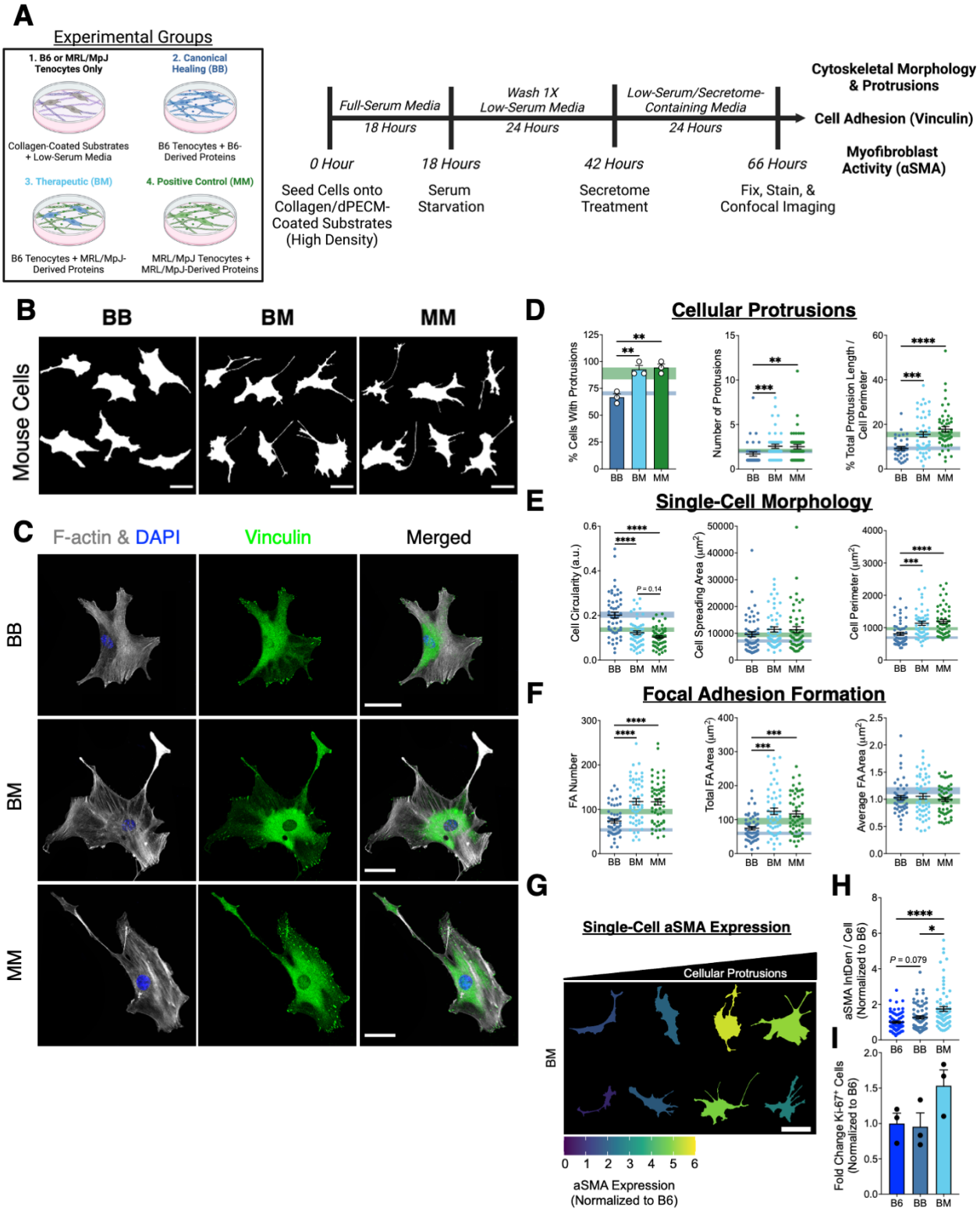
A
Experimental Groups
1. B6 or MRL/MpJ Tenocytes Only
2. Canonical Healing (BB)
Collagen-Coated Substrates + Low-Serum Media
B6 Tenocytes + B6-Derived Proteins
3. Therapeutic (BM)
4. Positive Control (MM)
B6 Tenocytes + MRL/MpJ-Derived Proteins
MRL/MpJ Tenocytes + MRL/MpJ-Derived Proteins
Full-Serum Media
18 Hours
Wash 1X Low-Serum Media
24 Hours
Low-Serum/Secretome-Containing Media
24 Hours
0 Hour
18 Hours
42 Hours
66 Hours
Seed Cells onto Collagen/dPECM-Coated Substrates (High Density)
Serum Starvation
Secretome Treatment
Fix, Stain, & Confocal Imaging
Cytoskeletal Morphology & Protrusions
Cell Adhesion (Vinculin)
Myofibroblast Activity (αSMA)
B
BB
BM
MM
Mouse Cells
C
F-actin & DAPI
Vinculin
Merged
D
Cellular Protrusions
% Cells With Protrusions
Number of Protrusions
% Total Protrusion Length / Cell Perimeter
E
Single-Cell Morphology
Cell Circularity (a.u.)
Cell Spreading Area (μm²)
Cell Perimeter (μm²)
P = 0.14
F
Focal Adhesion Formation
FA Number
Total FA Area (μm²)
Average FA Area (μm²)
G
Single-Cell aSMA Expression
Cellular Protrusions
aSMA Expression (Normalized to B6)
H
aSMA IntDen / Cell (Normalized to B6)
P = 0.079
I
Fold Change Ki-67⁺ Cells (Normalized to B6)

1405 **Fig. 6. Combination of MRL/MpJ-derived components modulate confluent B6**
1406 **tenocytes toward an MRL/MpJ-like regenerative phenotype *in vitro*.** (**A**)
1407 Experimental design and *in vitro* culture model of confluent cell experiments for
1408 tenocytes cultured with mouse-derived components for 7 days. (**B**) MRL/MpJ
1409 tenocytes maintained significantly greater F-actin alignment and ECM deposition
1410 than B6 tenocytes under serum-deprived culture conditions. However, Cx-43
1411 levels were significantly downregulated in MRL/MpJ tenocytes compared to B6
1412 tenocytes. (**C**) IF staining of F-actin (grey), fibronectin (green), and Cx-43
1413 (magenta) of confluent B6 and MRL/MpJ tenocytes treated with only MRL/MpJ
1414 dPECM, only MRL/MpJ secretome, or a combination of mouse-derived
1415 components for 7 days (scale bar, 100 μm). A polygonal, epithelial cell-like
1416 morphology was observed in B6 tenocytes treated with B6-derived components
1417 (indicated by yellow arrowheads). (**D**) B6 and MRL/MpJ tenocytes treated with
1418 MRL/MpJ-derived components exhibited comparable F-actin alignment and
1419 fibronectin deposition that were significantly greater than those of B6 tenocytes
1420 treated with B6-derived components. However, both treated B6 tenocyte groups
1421 had significantly lower Cx-43 levels compared to MRL/MpJ tenocytes treated with
1422 MRL/MpJ-derived components. (**E**) There was a combined benefit of treating B6
1423 tenocytes with both the MRL/MpJ dPECM and secretome on F-actin alignment,
1424 fibronectin deposition, and Cx-43 levels compared to either component alone. (**F**)
1425 Experimental design to quantify cellular senescence in tenocytes cultured with
1426 mouse-derived components for 3 days. MRL/MpJ components were unable to
1427 attenuate the onset of B6 tenocyte senescence/accumulation of ß-gal activity after
1428 48 hours of treatment. (**G**) B6 tenocytes treated with MRL/MpJ-derived
1429 components displayed a smaller proportion of senescent cells due to significantly
1430 increased total cell number compared to either component alone as well as B6
1431 tenocytes treated with B6-derived components. *$P < 0.05$, **$P < 0.01$, ***$P <$
1432 0.001, ****$P < 0.0001$. Significance was determined using a one-way ANOVA
1433 with post-hoc Tukey. Representative images shown for all staining experiments.
1434

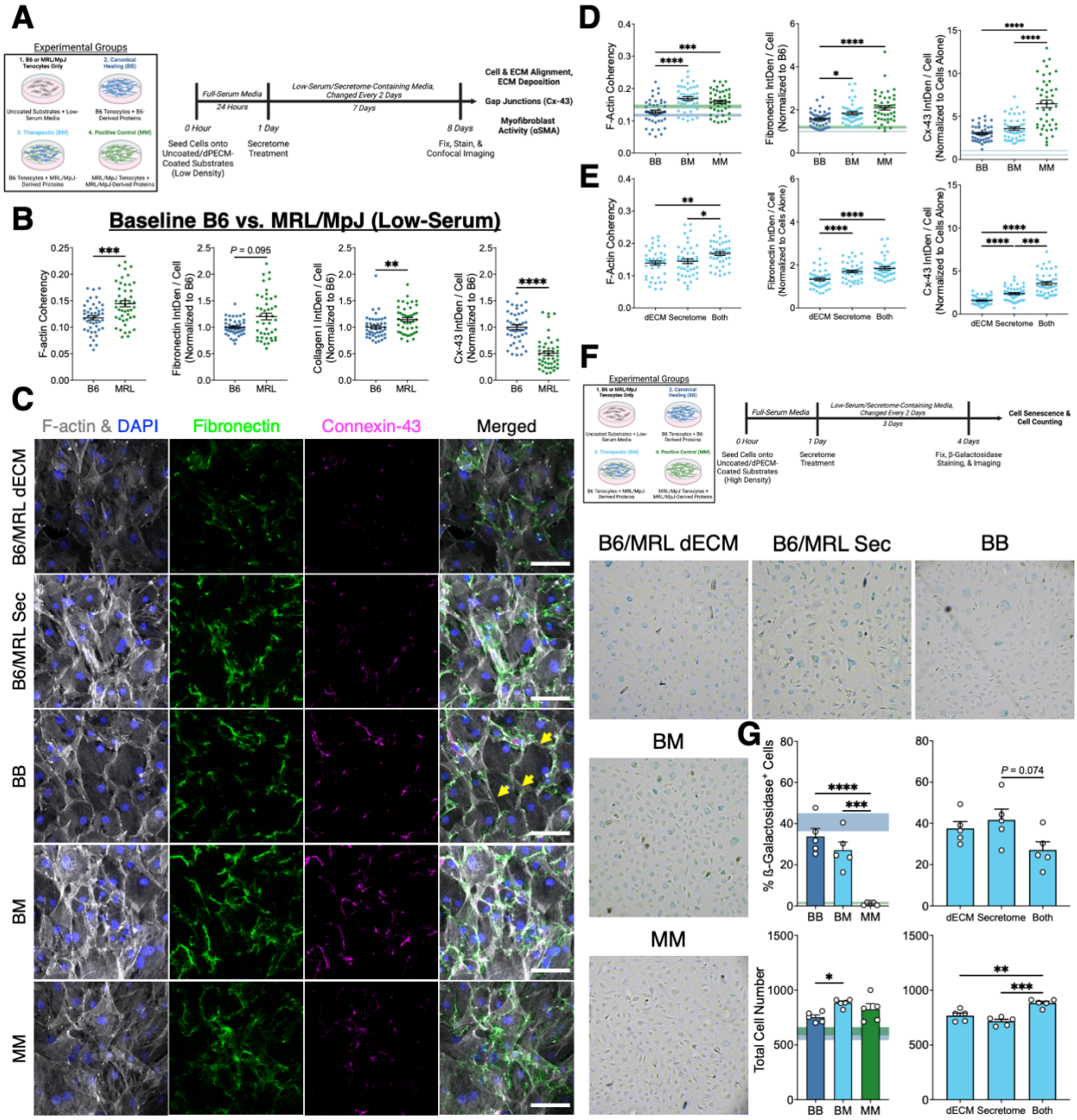
A
Experimental Groups
1. B6 or MRL/MpJ Tenocytes Only
2. Canonical Healing (BB)
3. Therapeutic (BM)
4. Positive Control (MM)
Uncoated Substrates + Low-Serum Media
B6 Tenocytes + B6-Derived Proteins
B6 Tenocytes + MRL/MpJ-Derived Proteins
MRL/MpJ Tenocytes + MRL/MpJ-Derived Proteins
Full-Serum Media
24 Hours
Low-Serum/Secretome-Containing Media, Changed Every 2 Days
7 Days
0 Hour
Seed Cells onto Uncoated/dPECM-Coated Substrates (Low Density)
1 Day
Secretome Treatment
8 Days
Fix, Stain, & Confocal Imaging
Cell & ECM Alignment, ECM Deposition
Gap Junctions (Cx-43)
Myofibroblast Activity (αSMA)
B
Baseline B6 vs. MRL/MpJ (Low-Serum)
F-actin Coherency
Fibronectin IntDen / Cell (Normalized to B6)
Collagen I IntDen / Cell (Normalized to B6)
Cx-43 IntDen / Cell (Normalized to B6)
P = 0.095
B6
MRL
C
F-actin & DAPI
Fibronectin
Connexin-43
Merged
B6/MRL dECM
B6/MRL Sec
BB
BM
MM
D
E
dECM
Secretome
Both
Cx-43 IntDen / Cell (Normalized to Cells Alone)
F
Experimental Groups
Full-Serum Media
Low-Serum/Secretome-Containing Media, Changed Every 2 Days
3 Days
4 Days
Seed Cells onto Uncoated/dPECM-Coated Substrates (High Density)
Secretome Treatment
Fix, β-Galactosidase Staining, & Imaging
Cell Senescence & Cell Counting
B6/MRL dECM
B6/MRL Sec
BB
BM
MM
G
% ß-Galactosidase+ Cells
Total Cell Number
P = 0.074

1450 **Fig. 7. A recombinant protein therapeutic comprised of MRL/MpJ-enriched**
1451 **structural and soluble factors phenocopies MRL/MpJ cell behavior in**
1452 **Sprague-Dawley rat tenocytes *in vitro***. (**A**) Experimental design of recombinant
1453 protein therapeutic development and *in vitro* culture model for single-cell and
1454 confluent cell experiments. (**B**) Representative cell outlines of Sprague-Dawley
1455 (SD) rat tenocytes cultured with B6 or MRL/MpJ-derived components or the
1456 recombinant protein therapeutic (scale bar, 100 μm) to visualize cytoskeletal
1457 morphology and cellular protrusions. (**C and D**) SD tenocytes treated with
1458 MRL/MpJ-derived components and the recombinant protein therapeutic exhibited
1459 identical (or superior in the protein therapeutic) cellular protrusion characteristics
1460 (C) and single-cell morphology (D) that were significantly different from SD
1461 tenocytes treated with B6-derived components. (**E**) IF staining of F-actin (grey)
1462 and fibronectin (green) of confluent SD tenocytes treated with mouse-derived
1463 components or the recombinant protein therapeutic (scale bar, 100 μm). (**F**) SD
1464 tenocytes treated with the recombinant protein therapeutic showed significantly
1465 higher F-actin alignment and similar fibronectin deposition compared to SD
1466 tenocytes treated with mouse-derived components. Total cell number was
1467 significantly reduced by the recombinant protein therapeutic relative to the
1468 MRL/MpJ-derived components. $^{*}P < 0.05$, $^{**}P < 0.01$, $^{***}P < 0.001$, $^{****}P <$
1469 0.0001. Significance was determined using a one-way Welch's ANOVA with post-
1470 hoc Games-Howell for cell morphology, total protrusion length, and total cell
1471 number data. For cellular protrusion and fibronectin deposition data, significance
1472 was determined using a one-way ANOVA with post-hoc Tukey (percentage of
1473 cells with protrusions) or Kruskal-Wallis test with post-hoc Dunn's (number of
1474 protrusions, normalized total protrusion length, normalized fibronectin integrated
1475 density). Representative images shown for all staining experiments.
1476

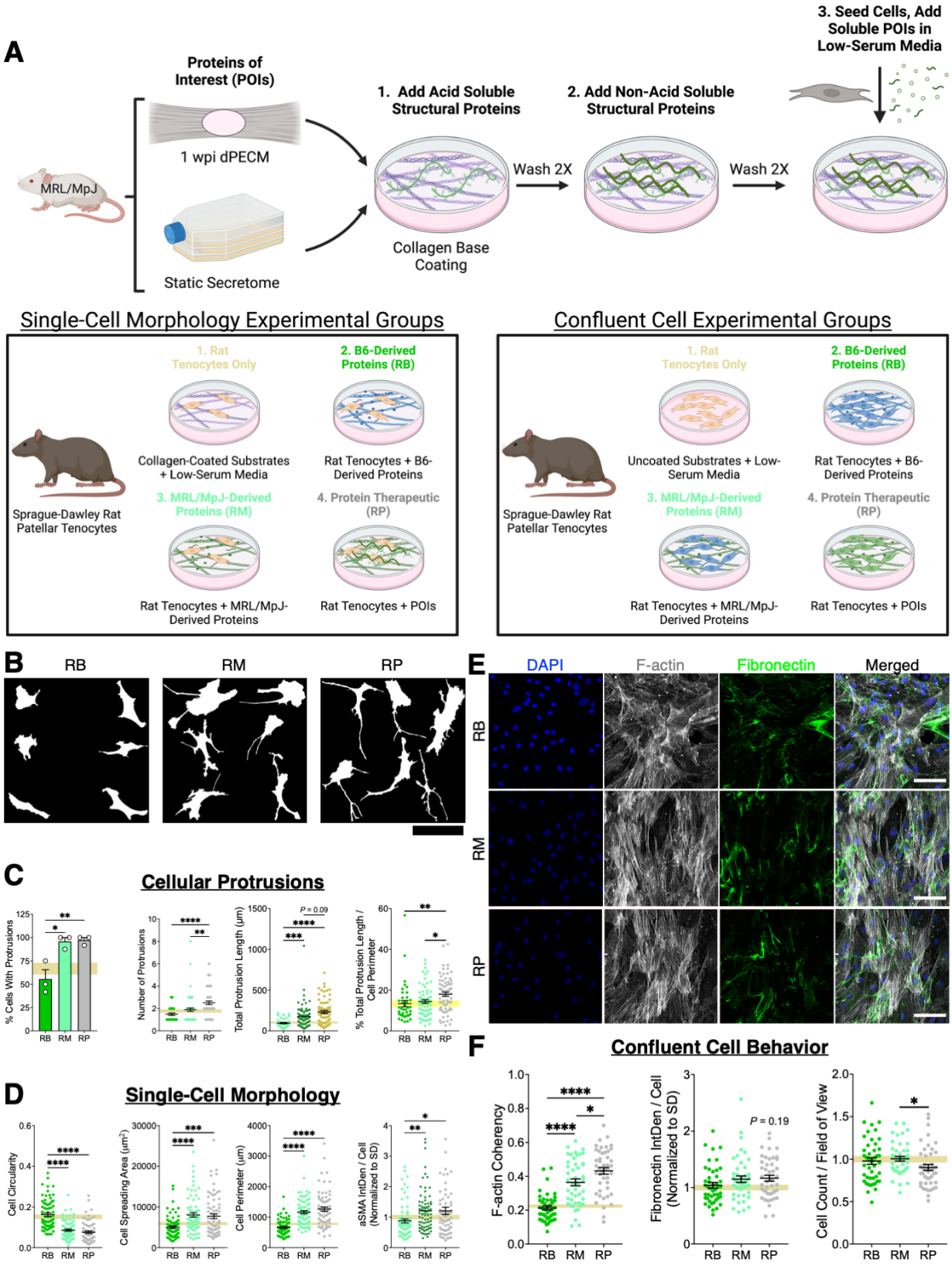
A
Proteins of Interest (POIs)
1 wpi dPECM
MRL/MpJ
Static Secretome
1. Add Acid Soluble Structural Proteins
Collagen Base Coating
Wash 2X
2. Add Non-Acid Soluble Structural Proteins
Wash 2X
3. Seed Cells, Add Soluble POIs in Low-Serum Media
Single-Cell Morphology Experimental Groups
1. Rat Tenocytes Only
2. B6-Derived Proteins (RB)
Collagen-Coated Substrates + Low-Serum Media
Rat Tenocytes + B6-Derived Proteins
3. MRL/MpJ-Derived Proteins (RM)
4. Protein Therapeutic (RP)
Sprague-Dawley Rat Patellar Tenocytes
Rat Tenocytes + MRL/MpJ-Derived Proteins
Rat Tenocytes + POIs
Confluent Cell Experimental Groups
1. Rat Tenocytes Only
2. B6-Derived Proteins (RB)
Uncoated Substrates + Low-Serum Media
Rat Tenocytes + B6-Derived Proteins
3. MRL/MpJ-Derived Proteins (RM)
4. Protein Therapeutic (RP)
Sprague-Dawley Rat Patellar Tenocytes
Rat Tenocytes + MRL/MpJ-Derived Proteins
Rat Tenocytes + POIs
B
RB
RM
RP
C
Cellular Protrusions
% Cells With Protrusions
Number of Protrusions
Total Protrusion Length (μm)
% Total Protrusion Length / Cell Perimeter
P = 0.09
D
Single-Cell Morphology
Cell Circularity
Cell Spreading Area (μm²)
Cell Perimeter (μm)
aSMA IntDen / Cell (Normalized to SD)
E
DAPI
F-actin
Fibronectin
Merged
F
Confluent Cell Behavior
F-actin Coherency
Fibronectin IntDen / Cell (Normalized to SD)
P = 0.19
Cell Count / Field of View

1484 **Table 1. Structural and soluble recombinant proteins enriched in the MRL/MpJ**
1485 **provisional extracellular matrix and secretome identified using quantitative**
1486 **proteomics**.

Role	Protein Name	Company	Product	Concentration (µg/mL)
Base	**Collagen, type I, alpha 1 (Col1a1)**	**Thermo Fisher Scientific**	**A1048301**	**500**
Structural Proteins (ECM Coating)	**Collagen, type VI, alpha 1 (Col6a1)**	**MyBioSource**	**MBS2105170**	**0.1**
	Collagen, type VI, alpha 3 (Col6a3)	**MyBioSource**	**MBS634441**	**0.1**
	Decorin	**R&D Systems**	**1060-DE**	**1**
	Fibrillin	**GeneTex**	**GTX00048-PRO**	**0.25**
	Fibrinogen	**LSBio**	**LS-G13486**	**100**
	Fibronectin	**Thermo Fisher Scientific**	**33-016-015**	**10**
	Inter-alpha-trypsin inhibitor heavy chain 1 (ITIH1)*	MyBioSource	MBS2009485	10
	Inter-alpha-trypsin inhibitor heavy chain 1 (ITIH3)*	Aviva Systems Biology	OPCA263725	10
	Periostin*			1
	Transforming growth factor βigh3 (TGFβigh3)	**R&D Systems**	**2559-BG**	**1**
Soluble Proteins (Exogenous Media Supplement)	Annexin A1 (ANXA1)*	Genetex	GTX00335	0.25
	Annexin A5 (ANXA5)*	LSBio	LS-G11883	0.25
	Annexin A6 (ANXA6)*	Sino Biological	11161-H08E	0.25
	CXCL1 (KC)	**R&D Systems**	**453-KC**	**0.01**
	CXCL5 (LIX)	**R&D Systems**	**433-MC**	**0.02**
	Epiregulin (EREG)	**Sino Biological**	**50559-M01H**	**0.0005**
	Fatty-acid-binding protein 4 (FABP4)	**R&D Systems**	**9840-CL**	**0.02**
	Follistatin (FST)	**Sino Biological**	**50035-M02S**	**0.1**
	Follistatin-like 1 (FSTL1)*	Sino Biological	51127-M02H	1
	Hepatocyte growth factor (HGF)	**Sino Biological**	**50038-MNAH**	**0.04**
	Interleukin 1 receptor antagonist (IL-1Ra)	MyBioSource	MBS2097334	
	Leptin	**R&D Systems**	**498-OB**	**0.001**

	Matrilin-2 (MATN2)	**R&D Systems**	**3234-MN**	**0.05**
	Matrix metalloproteinase-3 (MMP3)	**R&D Systems**	**548-MM**	**0.001**
	Protein disulfide-isomerase A3 (PDIA3)*	Novus Biologicals	NBP2-59883	3
	Prolyl isomerase (PPIase)*	Sino Biological	50296-M08E	0.5
	Peroxiredoxin 1 (PRDX1)*	MyBioSource	MBS206323	5
	S100-A11*	Sino Biological	50227-M07E	1
	Semaphorin 3F (SEMA3F)	**R&D Systems**	**3237-S3**	**0.05**

1487
1488 Bolded rows indicate the preliminary panel of 17 recombinant proteins that were
1489 evaluated in the present study.
1490
1491 *Indicates a protein that was unavailable at the time of experimentation and consequently
1492 was not evaluated in the present study.

1493 **Table 2. Top 30 activated and inhibited ingenuity pathway analysis upstream**
1494 **regulators from proteomic analyses of the static secretome**

Upstream Regulator	Molecule Type	Predicated Activation State	Activation Z-Score	*P* Value of Overlap
Activated in MRL/MpJ Secretome (Inhibited in B6 Secretome)				
ATP	chemical - endogenous mammalian	Activated	3.379	2.13E-11
FOS	transcription regulator	Activated	3.2	2.66E-21
ANGPT2	growth factor	Activated	3.086	1.04E-10
CG	complex	Activated	3.059	1.71E-17
cigarette smoke	chemical toxicant	Activated	3.034	2.35E-09
RORC	ligand-dependent nuclear receptor	Activated	2.8	4.95E-06
D-fructose	chemical - endogenous mammalian	Activated	2.791	2.21E-08
MTOR	kinase	Activated	2.758	8.07E-06
5-hydroxytryptamine	chemical - endogenous mammalian	Activated	2.722	3.73E-04
RAC1	enzyme	Activated	2.674	2.34E-09
TGFA	growth factor	Activated	2.622	3.20E-09
OLR1	transmembrane receptor	Activated	2.607	1.80E-08
S-nitroso-N-acetyl-DL-penicillamine	chemical reagent	Activated	2.596	2.91E-06
RIPK2	kinase	Activated	2.596	9.74E-08
JUN	transcription regulator	Activated	2.574	4.21E-25
ERK	group	Activated	2.56	3.21E-12
HRAS	enzyme	Activated	2.528	1.15E-15
IL10RA	transmembrane receptor	Activated	2.475	1.19E-19
dextran sulfate	chemical drug	Activated	2.448	1.14E-25
RETN	other	Activated	2.446	4.29E-09
F10	peptidase	Activated	2.429	2.84E-08
PTPN1	phosphatase	Activated	2.414	1.49E-05
UTP	chemical - endogenous mammalian	Activated	2.411	2.38E-06
EPHX2	enzyme	Activated	2.4	7.39E-08
collagenase	group	Activated	2.36	6.75E-10
Collagen type II	complex	Activated	2.357	1.35E-12

cisplatin	chemical drug	Activated	2.353	5.26E-12
5-O-mycolyl-beta-araf-(1->2)-5-O-mycolyl-alpha-araf-(1->1')-glycerol	chemical - endogenous non-mammalian	Activated	2.339	4.95E-06
NFKBIB	transcription regulator	Activated	2.306	1.93E-11
PTX3	other	Activated	2.304	1.31E-08
Inhibited in MRL/MpJ Secretome (Activated in B6 Secretome)				
DUSP1	phosphatase	Inhibited	-3.348	1.24E-13
vitamin E	chemical drug	Inhibited	-3.265	4.17E-09
beta-estradiol	chemical - endogenous mammalian	Inhibited	-3.128	4.84E-28
SB-431542	chemical reagent	Inhibited	-2.884	5.93E-11
UCP1	transporter	Inhibited	-2.813	3.28E-03
estrogen receptor	group	Inhibited	-2.782	1.51E-14
MEOX2	transcription regulator	Inhibited	-2.722	7.88E-12
ESR1	ligand-dependent nuclear receptor	Inhibited	-2.708	5.43E-13
NOTCH2	transcription regulator	Inhibited	-2.588	5.77E-06
genistein	chemical drug	Inhibited	-2.568	4.45E-16
STK11	kinase	Inhibited	-2.53	4.81E-10
INPP5D	phosphatase	Inhibited	-2.456	1.56E-06
pimagedine	chemical drug	Inhibited	-2.449	1.87E-06
MSC	transcription regulator	Inhibited	-2.449	2.00E-04
FBXO32	enzyme	Inhibited	-2.438	1.60E-03
diphenyleneiodonium	chemical reagent	Inhibited	-2.428	4.09E-08
actinomycin D	biologic drug	Inhibited	-2.421	3.18E-16
TAF4	transcription regulator	Inhibited	-2.412	1.78E-08
Traj18	other	Inhibited	-2.401	4.54E-09
CHRNA7	transmembrane receptor	Inhibited	-2.397	9.90E-06
tosylphenylalanyl chloromethyl ketone	chemical - protease inhibitor	Inhibited	-2.395	1.46E-06

SB203580	chemical drug	Inhibited	-2.388	6.20E-24
Y 27632	chemical drug	Inhibited	-2.384	9.29E-11
metformin	chemical drug	Inhibited	-2.375	3.08E-08
Hbb-b1	transporter	Inhibited	-2.359	1.04E-05
TET2	enzyme	Inhibited	-2.353	2.87E-04
tempol	chemical drug	Inhibited	-2.345	3.63E-09
Sb202190	chemical drug	Inhibited	-2.342	1.02E-07
APC	enzyme	Inhibited	-2.338	1.79E-14
caffeic acid phenethyl ester	chemical drug	Inhibited	-2.336	8.03E-10

1495

1496 **Table 3. Increased and decreased ingenuity pathway diseases and functions from**
1497 **proteomic analyses of the static secretome**
1498

Diseases or Function Annotation	Categories	Predicated Activation State	Activation Z-Score	*P* Value of Overlap
Increased in MRL/MpJ Secretome (Decreased in B6 Secretome) – 8 Total				
Mitogenesis	Cell Cycle	Increased	2.794	1.61E-31
Angiogenesis of lesion	Organismal Injury and Abnormalities	Increased	2.459	2.62E-21
Invasion of malignant tumor	Cancer, Organismal Injury and Abnormalities, Tumor Morphology	Increased	2.343	7.61E-23
Organismal death	Organismal Survival	Increased	2.286	4.16E-39
Morbidity or mortality	Organismal Survival	Increased	2.203	7.78E-42
Binding of breast cancer cell lines	Cell-To-Cell Signaling and Interaction	Increased	2.166	4.24E-26
Migration of vascular cells	Cellular Movement	Increased	2.028	3.10E-26
Invasion of tumor	Cancer, Organismal Injury and Abnormalities, Tumor Morphology	Increased	2.004	3.31E-25
Decreased in MRL/MpJ Secretome (Increased in B6 Secretome) – 11 Total				
Cytotoxicity of lymphatic system cells	Cell Death and Survival, Cellular Compromise	Decreased	-2.434	1.08E-29
Cytotoxicity of cells	Cell Death and Survival, Cellular Compromise	Decreased	-2.349	2.23E-26
Toxicity of cells	Cell Death and Survival, Cellular Compromise	Decreased	-2.315	3.81E-28
Cytotoxicity of lymphocytes	Cell Death and Survival, Cellular Compromise	Decreased	-2.313	1.03E-28
Expansion of T lymphocytes	Cellular Development, Cellular Growth and Proliferation, Hematological System Development and Function, Lymphoid Tissue Structure and Development	Decreased	-2.268	5.76E-27

Cytotoxicity	Cell Death and Survival	Decreased	-2.166	3.32E-29
Cell movement of T lymphocytes	Cell-mediated Immune Response, Cellular Movement, Hematological System Development and Function, Immune Cell Trafficking	Decreased	-2.135	1.80E-35
T cell migration	Cell-mediated Immune Response, Cellular Movement, Hematological System Development and Function, Immune Cell Trafficking	Decreased	-2.116	5.83E-35
Expansion of lymphatic system cells	Cellular Growth and Proliferation, Lymphoid Tissue Structure and Development	Decreased	-2.09	9.39E-34
MAPKKK cascade	Cell Signaling	Decreased	-2.075	5.82E-30
Cell movement of macrophages	Cellular Movement, Hematological System Development and Function, Immune Cell Trafficking, Inflammatory Response	Decreased	-2.03	2.35E-41

1499

1500